Materials & Design 213 (2022) 110345

Contents lists available at ScienceDirect

Materials & Design

journal homepage: www.elsevier.com/locate/matdes

Towards an instant structure-property prediction quality control tool for additive manufactured steel using a crystal plasticity trained deep learning surrogate

Yuhui Tu [a,b,f], Zhongzhou Liu [c], Luiz Carneiro [d], Caitriona M. Ryan [b,e], Andrew C. Parnell [b,e], Seán B Leen [a,b,f], Noel M Harrison [a,b,f,*]

[a] Mechanical Engineering, National University of Ireland, Galway, Ireland
[b] I-Form Advanced Manufacturing Research Centre, Ireland
[c] School of Computing and Information Systems, Singapore Management University, Singapore
[d] Department of Mechanical Engineering, University of Nevada, Reno, NV 89557, USA
[e] Hamilton Institute, Maynooth University, Ireland
[f] Ryan Institute for Environmental, Marine and Energy Research, NUI Galway, Ireland

GRAPHICAL ABSTRACT

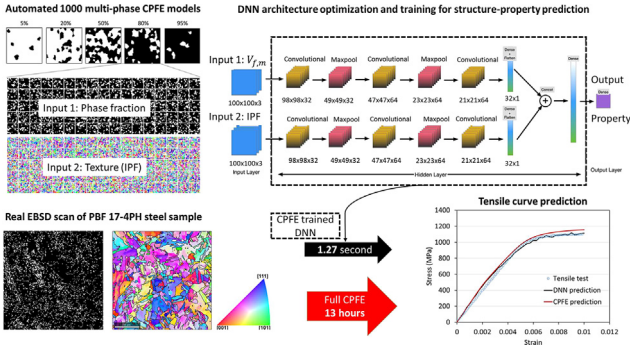

ARTICLE INFO

Article history:
Received 23 September 2021
Revised 1 December 2021
Accepted 21 December 2021
Available online 22 December 2021

Keyword:
Crystal plasticity
Deep neural network
17-4PH stainless steel
Additive manufacturing
Micromechanics

ABSTRACT

The ability to conduct in-situ real-time process-structure-property checks has the potential to overcome process and material uncertainties, which are key obstacles to improved uptake of metal powder bed fusion in industry. Efforts are underway for live process monitoring such as thermal and image-based data gathering for every layer printed. Current crystal plasticity finite element (CPFE) modelling is capable of predicting the associated strength based on a microstructural image and material data but is computationally expensive. This work utilizes a large database of input–output samples from CPFE modelling to develop a trained deep neural network (DNN) model which instantly estimates the output (strength prediction) associated with a given input (microstructure) of multi-phase additive manufactured stainless steels. The DNN model successfully recognizes phase regions and the associated unique crystallographic orientation variations. It also captures differences in macroscopic stress response due to the varying microstructure. However, it is less reliable in terms of fatigue life predictions. The DNN model

Abbreviations: PBF, powder bed fusion; CPFE, crystal plasticity finite element; EBSD, electron backscatter diffraction; RVE, representative volume element; VT, Voronoi tessellation; AM, additive manufacturing; DL, deep learning; CNN, convolutional neural network; DNN, deep neural network; PBC, periodic boundary condition; $V_{f,m}$, Martensite volume fraction; FIPs, fatigue indicator parameters; MAE, mean absolute error; MSE, mean squared error; BP, back propagation; YS, yield stress.

* Corresponding author at: Mechanical Engineering, National University of Ireland, Galway, Ireland.
E-mail addresses: y.tu2@nuigalway.ie (Y. Tu), zzliu.2020@smu.edu.sg (Z. Liu), lcarneiro@nevada.unr.edu (L. Carneiro), triona.Ryan@mu.ie (C.M. Ryan), andrew.parnell@mu.ie (A.C. Parnell), sean.leen@nuigalway.ie (S.B Leen), noel.harrison@nuigalway.ie (N.M Harrison).

https://doi.org/10.1016/j.matdes.2021.110345
0264-1275/

Nomenclature

$\dot{\gamma}^{\alpha}$	rate of slip along the slip system α
α	current slip system
$\dot{a}$	reference strain rate component [s^{-1}]
n	strain rate sensitivity
τ^{α}	slip system resolved shear stress [MPa]
g^{α}	isotropic strain hardening coefficient [MPa]
g_0	initial critical resolved shear stress [MPa]
g_{∞}	stage I stress [MPa]
h_0	self-hardening moduli [MPa]
x^{α}	kinematic hardening back stress [MPa]
C_{11}, C_{12}, C_{44}	elastic anisotropic constants [GPa]
C_1, D_1	Armstrong-Frederick parameters for the back-stress evaluation [GPa]
b	fatigue equation exponent
p	accumulated effective crystallographic slip
W	accumulated crystallographic strain energy dissipation [MJ/m^{-3}]
N_i	fatigue crack initiation life

exhibits high accuracy for the structure–property relationship as a surrogate prediction tool compared to CPFE while significantly reducing the computational cost to just a few seconds.

1. Introduction

The medical device and aerospace industries have led the adoption of metal powder bed fusion (PBF) additive manufacturing (AM) as a process of choice for next-generation manufacturing. However, challenges with real-time quality control and process-structure–property awareness limit further uptake of PBF. The mechanical performance of metals during in-service deformation is largely dependent on microstructural features such as phase composition, crystallographic orientation, grain morphology, as well as grain size distribution [1]. The complex layer-by-layer solidification process and intricate thermal history of metal PBF parts present difficulties in predicting the material microstructure of printed parts. Such structure and performance predictive capability has not been developed in a format suitable for industrial quality control or live process optimization, in part because of the lack of high-resolution in-situ PBF microscopy technology.

Finite element analysis, involving grain boundary and crystal orientation specifications, along with constitutive and damage model parameters, are referred to as crystal plasticity finite element (CPFE) methods [2–5]. CPFE modelling has been utilized to quantify the phase composition effect on tensile behaviour [6,7], the higher ductility and strength caused by finer grain size structure [8,9], the strengthening effect of grain boundaries [10,11], as well as manufacturing direction-induced texture effect [12,13]. This predictive capability has been applied to investigate AM metals and processes within manufacturing and materials research, requiring post-build sectioning, polishing, imaging, model reconstruction and time-consuming analysis.

Most CPFE studies are based on Voronoi tessellation (VT) idealised (grain morphology and linear grain boundaries) representative volume elements (RVE) that statistically represent the real microstructure [14–16]. Other recent CPFE studies have introduced high-fidelity models based on realistic characterization images from scanning electron microscope (SEM) or electron backscatter diffraction (EBSD) scans [17–19]. The difficulty in determining accurate minor phase content (below 10%) has led some researchers to approximate dual phase materials as single phase (Ti-6Al-4V [20], 316L steel [21] and P91 steel [22]), though dual phase CPFE studies on AM Ti-6Al-4V [6,20] have been reported.

CPFE methods have evolved to include increased slip system complexity [23,24], allowing simulation of multi-phase alloy behaviour. These advances improve accuracy and broaden the applicability, but they also increase computational cost. This computational effort increases when the loading condition is complex (e.g. cyclic) and further grows if a definitive RVE model [25,26] or a high-fidelity model (realistic microscopy image based) is required. Such advanced modelling generally requires model development and simulation time in the order of hours and days, respectively. Often high-end computer infrastructure is required to perform the computation, and once complete offers powerful insights into the contribution that individual microstructural features make to the local and bulk material response. While accurate and insightful, CPFE is far removed from a live in-process property predictive tool, primarily due to model setup and simulation times.

Stainless steels have emerged as a common material for metal printing due to the low power requirement for melting and the non-reactive properties of the material in powder form [27]. The AM fabricated stainless steel exhibits different phase components (austenite, martensite, and ferrite), leading to a complex combination of microstructure and mechanical properties [1]. Studies have shown that chemical phase fraction has a bigger influence on mechanical behaviour, among a range of microstructural features examined in PBF additive manufactured 17-4PH stainless steel (SS17-4PH) and 316L stainless steel (SS316L) [28]. SS17-4PH is a dual-phase steel strengthened by precipitation. As-built SS17-4PH contains mainly martensite phase together with the retained austenite phase [29], the precise fraction of which is highly dependent on the PBF process as well as post heat treatment parameters [30]. Studies have reported the retained austenite phase varying from 3% to 63% [31–34]. Similar behaviour was also observed for other stainless steels such as SS316L, with the detected volume fraction of ferrite ranging from 0.83% to 7.83% [35,36]. Variations in PBF process parameters, number of parts in a build or build layouts can lead to variations in as-built microstructure, and consequently variations in local mechanical performance [37]. Even when process parameters are held constant in a build, a gradient in microstructure can often be observed along the build direction [38]. This, along with the risk of defect occurrence, has led to some PBF equipment manufacturers developing live process monitoring quality tools that image and record sensor data for each individual solidified layer, before the next layer of loose powder is applied. As optical imaging resolution and sensor technology continue to advance, it is anticipated that the next generation of quality control

in PBF machines will go beyond melt-pool analysis and record as-solidified microstructural features, such as grain boundaries within the captured individual layer data. To take advantage of this live microstructural data, an ideal in-process PBF monitoring tool should have a structure–property prediction for each printed layer. However, live-CPFE modelling of the individual layers is impractical due to computational cost and the short time frame (generally seconds) between successive layer printing.

Over recent years, Deep Learning (DL), a subclass of the general term machine learning, has become a popular tool due to its ability to deal with big data efficiently. DL provides greater flexibility via an artificial neural network where successive transformations (known as hidden layers) of the inputs extract useful information from the previous layers to predict the final output, with minimal human bias. Some studies have considered integrating DL with the structure–property prediction models to either assist decision making [39–42] and non-destructive quality control [43,44], or improve efficiency [45,46]. Such existing DNN-CPFE coupled methods focus on stress–strain behaviour prediction and computational cost reduction. Convolutional neural networks (CNN)was adopted as the encoder to study the crystallographic texture effect on the stress–strain behaviour [47] and orientation evolution [48] of a synthetic RVE morphology. CNN methods gave accurate predictions compared to CPFE simulations but in milliseconds. Yamanaka et al. [49] developed a DNN tool to read in 3D orientation information of aluminium sheet material and applied this to estimate the biaxial stress–strain behaviour. Mangal [50] used CNNs to predict stress localization and capture hotspots. While previous studies have successfully implemented DL techniques with various structure–property models, to the author's knowledge, an integrated DL-CPFE tool that captures the effect of phase and crystallographic orientation in AM materials has not been previously developed.

This study presents a data-driven DL model based on a CPFE predicted structure–property relationship database. This will provide an instant predictive capability to advance the development of a live process-structure–property tool based on real-time image and sensor data, giving real-time layer-by-layer strength predictions, once suitable in-situ microscopy technology is in place.

2. Methodology

The workflow is described in Fig. 1. This process firstly generates a statistically equivalent VT-generated CPFE model from the EBSD measurement of an AM 17-4PH stainless steel sample. The input parameters are calibrated against experimental stress–strain behaviour under tensile and cyclic fatigue conditions (ASTM-E606). The dual phase CPFE model is then extended to five different martensite volume fractions ($V_{f,m}$) model sets. Each set contains 200 models, with different (random) grain morphologies, leading to the simulation of 1000 unique CPFE models in total. The resulting 1000 structure–property linkages are used for training and validating the DL model as a surrogate tool for CPFE to rapidly predict structure–property relationships.

2.1. Material and experimental characterization

The material employed for this study is the AM SS17-4PH specimen [33] fabricated via PBF under the protection of argon atmosphere. The samples were built along the axial direction (vertically printed) where the deposited powder layer was perpendicular to the specimen axis. The PBF specimen was then subjected to the recommended post-build heat treatment. Post-build processing consisted of solution annealing at approximately 1050 °C, air cooling, and then age hardening at 593 °C for 4 h, followed by air cooling at room temperature. Grit blasting was conducted to improve the surface quality and the polished average surface roughness was measured as 60.1 μm. The specimen geometry design and the mechanical test protocol followed the ASTM E606 standard [51]. The as-built sample had a length of 16 mm and diameter of 8 mm at the gauge section, The shoulder radius of the testing specimen was 40 mm. The grip section had a diameter of 16 mm.

SEM and EBSD were used to scan the microstructure and reconstruct the grain map to measure phase information, as well as the orientation map. EBSD scans were taken using a Jeol JSM-7100F field emission SEM located at the University of Nevada, equipped with an Oxford EBSD detector. A microstructural sample was cut from the gauge area using a scan area of 300×300 μm and a step resolution of 0.5 μm to detect the austenite and martensite phases together with their crystallographic orientation texture. Axial tensile test and strain-controlled fatigue tests were conducted under ambient air conditions using a servo-hydraulic tension–torsion Instron load frame equipped with the 8800 controller. The test machine has a maximum loading force capacity of 222 kN to characterise the plasticity and fatigue behaviour of the SS17-4PH material and to facilitate constitutive behaviour calibration of the CPFE model. Both tests were equipped with an extensometer with a gauge length of 12.7 mm to monitor and measure the strain evolution. The tensile test was conducted under displacement control with an approximated strain rate of $8 \times 10^{-4}\ s^{-1}$. Fully reversed strain-controlled fatigue tests were conducted with the testing frequency from 0.2 Hz to 10 Hz according to the strain amplitude ranging from 1.5×10^{-3} to 1.0×10^{-2}. The strain limit is 40% in the monotonic tensile test and ±10% in the fatigue test. During individual cycles in the fatigue test, a minimum of 200 data points were recorded and the fatigue failure was considered to take place once the maximum stress was reduced by 5% compared to the stabilized peak value.

2.2. CPFE based dataset generation

The data-driven model requires structure–property relationship data for training the DNN model. In the absence of large datasets of experimental testing for structure–property relationships of PBF-LB manufactured stainless steel, CPFE models are adopted here as a reasonable method to produce a broad map of property-structure linkage information for the DL tool. The VT based grain maps were generated using DREAM3D [52]. The advantage of this tool is that it permits random grain nucleation while maintaining a constant phase fraction ratio. This feature is beneficial to imitate a batch of samples with the same print parameters.

An efficient simulation framework was developed to batch generate and solve large groups of dual-phase VT models automatically. Each model contains approximately 100 grains of average grain size 10.36 μm and each grain is meshed with approximately 100 linear solid hexahedral (C3D8) finite elements in the general purpose finite element solver ABAQUS [53]. This voxel mesh permits direct conversion from image pixels to a finite element mesh [54] and also facilitates a consistent DNN input size for all models thus minimizing the potential bias of DNN input size [55]. This three-dimensional solid element as a recommended stress/displacement element [56], has also been shown to have better accuracy compared to linear tetrahedron mesh for plasticity simulations [57]. 200 unique CPFE models were generated for each martensite volume fractions ($V_{f,m}$) of 5, 20, 50, 80, 95%, with a constant grain size distribution and phase fraction. Crystallographic orientation is assigned to individual grains according to the inverse pole figures (IPFs), to generate 1000 unique polycrystalline realizations in total. Fig. 2 shows sample models from the 80% $V_{f,m}$ model set. The martensite phase is shown in black with austenite in white

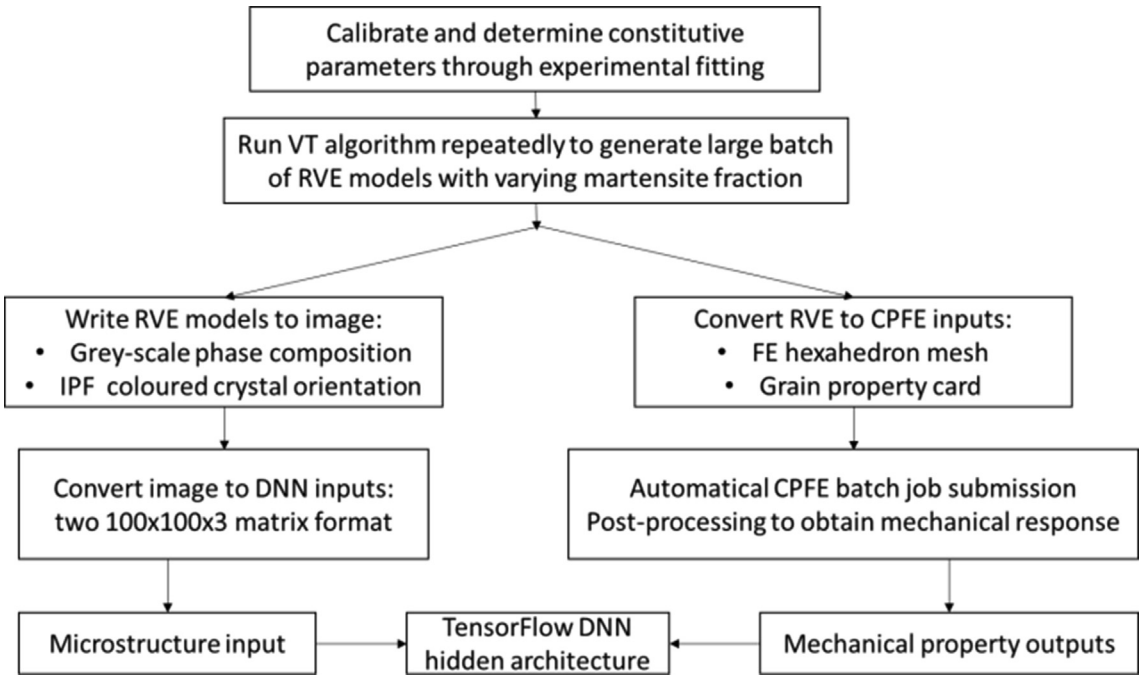

Fig. 1. Schematic of the integrated CPFE-DNN architecture, two images containing phase fraction and orientation information act as input to predict mechanical properties.

and corresponding grain morphology and orientation data shown in colour. Materials consisting of more than two phases would require a colour map for complete phase data description.

Periodic boundary conditions (PBC) [58] were applied to the free surfaces in the CPFE models together with a strain of 1.0%, which is sufficient to calculate bulk yield strength value while keeping an acceptable CPFE running time. A customized script was applied to schedule the job and perform results extraction once the simulation finishes. These post-processed property data (stress–strain and fatigue data) act as the output of the DNN model.

2.3. Crystal plasticity model

The CPFE model implements large deformation theory, and the deformation is determined by crystallographic slip only. Table 1 lists the calibrated constitutive parameters used in this paper.

The power law flow adopted here was first introduced by Huang [59] and improved by Sweeney [60] implementing an Armstrong–Frederick rule to describe non-linear kinematic hardening behaviour in fatigue problems:

$$\dot{\gamma}^{\alpha} = \dot{a} sgn(\tau^{\alpha} - x^{\alpha}) \left\{ \frac{|\tau^{\alpha} - x^{\alpha}|}{|g^{\alpha}|} \right\}^{n} \tag{1}$$

where $\dot{\gamma}^{\alpha}$ is the crystallographic slip rate on slip system α, $\dot{a}$ is the reference strain rate component, τ^{α} is the resolved shear stress of the slip system, n is rate sensitivity exponent, and g^{α} defines the isotropic strain hardening coefficient.

This dual phase CPFE model contains 24 slip systems, 12 for the FCC lattice structure austenite phase, and another 12 for the BCC martensite phase [61,62], shown in Fig. 3.

The hardening behaviour is described by:

$$\dot{x}_1^{\alpha} = C_1 \dot{\gamma}^{\alpha} - D_1 x_1^{\alpha} |\dot{\gamma}^{\alpha}| \tag{2}$$

where C_1 and D_1 together determine the back-stress evolution by controlling the rate of decay, for the simulation of kinematic hardening.

In order to predict the FCI life here, it is important to use a scale-consistent fatigue indicator parameter (FIP). In this case, based on previous work, two FIPs, namely accumulated effective crystallographic slip p [63], and cumulative energy dissipation W [64,65] were calculated. Eqs. (5)–(7) define the calculation of these two FIPs. The two FIPs have successfully been utilized in previous research [6,56] to determine fatigue crack initiation.

Accumulated effective crystal slip p, aggregated over all slip systems including the effects of mean stress, is successfully implemented with CPFE to predict fatigue behaviour as follows:

$$\dot{p} = \left(\frac{2}{3}\boldsymbol{L}^{\mathrm{p}} : \boldsymbol{L}^{\mathrm{p}}\right)^{\frac{1}{2}} \tag{3}$$

$$p = \int_0^t \dot{p} dt \tag{4}$$

Further development of this FCI prediction approach considers the accumulated strain energy dissipation parameter W which sums up the energy consumption on all the crystal slip systems by considering both microscale shear stress and slip rate, as follows:

$$W = \sum_{\alpha} \int_0^t \tau^{\alpha} \dot{\gamma}^{\alpha} dt \tag{5}$$

It has been found that the two FIPs tend to evolve and reach a stabilised value after a small number of cycles during CPFE modelling. Thus, it is reasonable to predict the numbers of cycles for FCI by dividing a critical FIP value FIP_{crit} by that of the stabilized fatigue cycle FIP_{cyc}, as shown below:

$$p_{\mathrm{cyc}} = p_t - p_{t-\Delta t_{cyc}} \tag{6}$$

$$W_{cyc} = W_t - W_{t-\Delta t_{cyc}} \tag{7}$$

$$N_{i,p} = \frac{p_{\mathrm{crit}}}{(p_{\mathrm{cyc}})^{b_1}} \tag{8}$$

$$N_{i,\,W} = \frac{W_{\mathrm{crit}}}{\left(W_{\mathrm{cyc}}\right)^{b_2}} \tag{9}$$

where Δt_{cyc} is the modelling time consumed to finish one fatigue cycle.

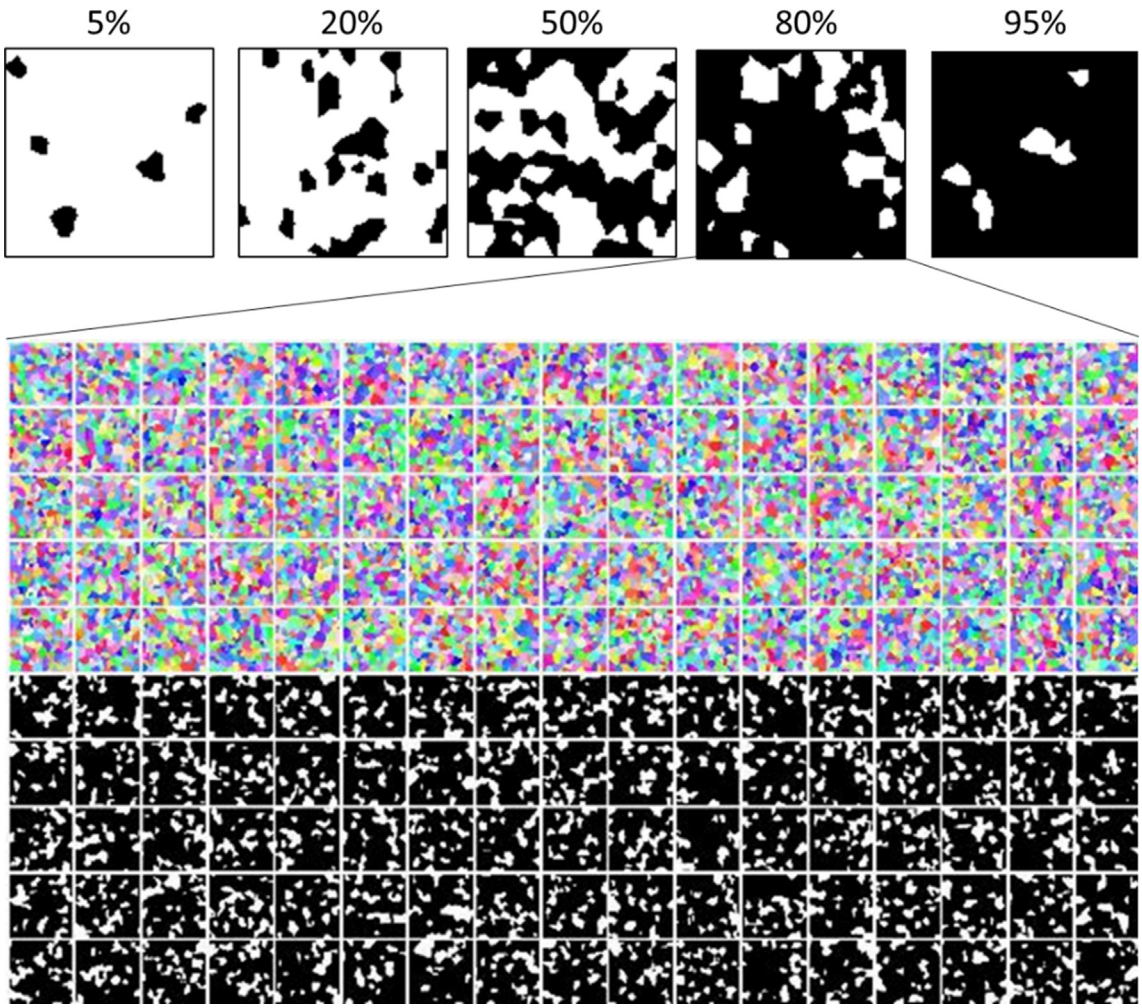

Fig. 2. A sample of 85 automatically generated CPFE big data generation results with unique grain morphology, crystallographic orientation and phase volume fraction information for five different martensite phase fractions. Each individual square represents a 100 × 100 μm sample.

Table 1
Calibrated parameters for dual phase CPFE model.

Parameter	Martensite BCC	Austenite FCC
$\dot{a}$	0.001 s^{-1}	0.001 s^{-1}
n	50	50
g_0	466 *MPa*	192.5
g_∞	740 *MPa*	402.5
h_0	20 *MPa*	20 *MPa*
C_{11}	262 *GPa*	204.6 *GPa*
C_{12}	150 *GPa*	137.7 *GPa*
C_{44}	112 *GPa*	126.2 *GPa*
C_1	10,000	
D_1	200	
b	1.58	

The critical FIP values are identified and validated by comparing the CPFE-predicted and measured FCI data for certain sample tests. The exponent b is solved through the experimental data-fitting process by a nonlinear least-squares algorithm. This power-law approach was considered necessary to improve the fatigue prediction [66–68].

The integrated algorithm was written in a user material subroutine (UMAT) [60] for ABAQUS. More details about self-hardening and latent-hardening moduli definitions can be found in prior literature [58,69,70].

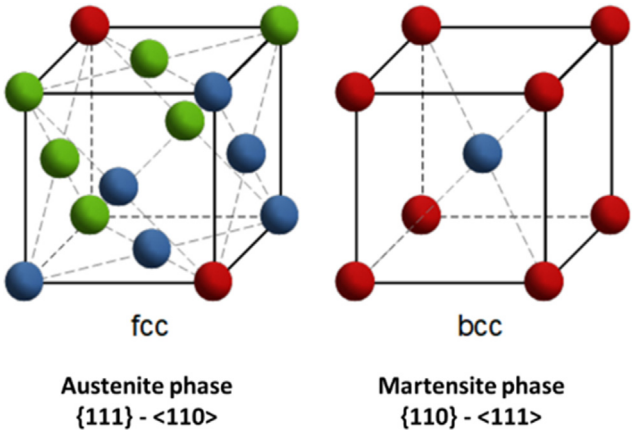

Fig. 3. Slip systems and crystallographic lattice of austenite and martensite phase.

2.4. Deep neural network model

2.4.1. Deep neural network architecture

The commonly used machine learning methodologies include DNNs, ANNs, SVMs, gradient boosting, and random forests etc. This work adopts the DNN approach as it has previously been shown to

be effective for image recognition and the labor-intensive process of feature engineering [71]. Specifically, the inputs of the DL model are the microstructural images containing phase and orientation data, and the output value is the predicted tensile stress–strain curve. The 100×100 pixel (nodes in CPFE) microstructural images, representing phase composition and orientation, were converted to DNN input data format, which contained the RGB values respectively, for the complete model. Thus, the phase map input and the orientation map use $100 \times 100 \times 3$ array sizes. A customized Python code was developed for calculating the macroscopic stress based on the CPFE-predicted reaction force, and the result together with its strain value, was recorded with an interval of 0.00025 strain. Consequently, 40 data points were extracted and used to plot the stress–strain curves, which also acted as the DNN output, with an array dimension of 40×2. In this work, two different types of DNN architecture are considered. A standard sequence DNN network [49,72] is firstly developed where inputs go through a single pipeline shown in Fig. 4 (a). As the microstructural inputs have two variables, the sequence DNN design may not be appropriate. Thus, an optimized non-sequence (Siamese) DNN structure [73] with two pipelines, shown in Fig. 4 (b), was also developed to capture the structural features of phase and crystallographic orientation (represented as IPF colour) data separately.

The base module of the DNN model implements TensorFlow and convolution neural networks (CNN) as the kernels to extract information from the microstructure images. CNN is generally designed to handle the problem of processing grid-shaped data which are difficult to process via traditional deep learning models. It utilizes several small filters and pooling layers to efficiently extract features which are useful for downstream tasks. Further general information on convolution layer design can be found elsewhere [74]. In this study, the design of the CNN contains the following layers: convolution layer [75], pooling layer and dropout layer.

The convolution layer only needs a small part for each computation (usually 3×3 or 5×5), resulting in a much smaller number of parameters. It consists of several filters which capture the distributions of the specific characteristic on the data (i.e. in which part the characteristic is more significant when predicting the result, also denoted by a weight parameter) by performing matrix multiplication with a part of the data. In this way, the filters are a set of matrices whose elements (parameters) are implicitly and automatically learned during the training process of model development. The stress–strain property of each instance is influenced by different characteristics of the data. The goal of the convolution layer is to determine the implicit characteristics that contribute to the stress property. The hyper-parameters were defined based on a (published) recommended stable value [76], without an explicit hyper-parameter search, as it was observed that the predicted output was not sensitive to minimal change in hyper-parameter.

Integrating the two different CNNs to extract the characteristic of phase and orientation separately while aggregating the outputs together at the last 3 layers (as shown in Fig. 4) is a key novelty in this study. In a standard sequence DNN design, the two images are usually imported at the first layer where rich semantic information could be lost. However, in the new model, by aggregating the images in the last 3 layers, it can better capture their common points and differentiate their features thus leading to an improved prediction [77].

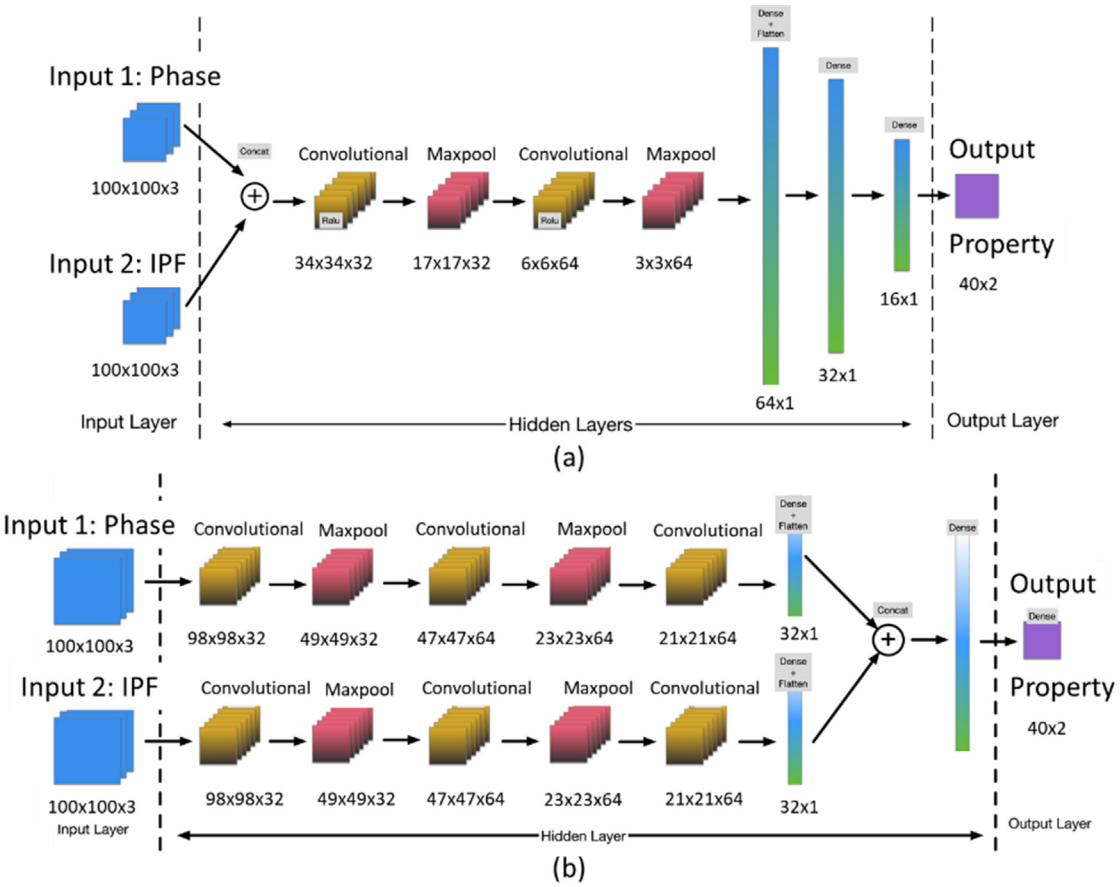

Fig. 4. (a) Single pipeline sequence DNN (before optimization) and (b) non-sequence multi-pipeline Siamese DNN (after optimization).

2.4.2. DNN model training and validation

The DNN inputs consist of 1000 varying microstructural images including phase and crystallographic orientation variations, each with 10,000 pixels, thus 2×10^7 data features in total. There is no fixed value for optimal ratio of size of training sample dataset to size of validation sample dataset, as this parameter depends on the signal-to-noise ratio in the data and the training sample size. The effect of this ratio selection has been discussed in a previous study [55], showing that an increase in the training set percentage can lead to an unstable estimation of the true performance of the DNN model, while a reduced training set percentage can lead to a poor model due to insufficient amount of training data. In this study, a range of ratios was examined, as shown in Table 2, where a training to validation ratio of 75:25 was found to give the lowest mean absolute error (MAE) in yield strength predictions. Consequently, the CPFE predicted 1000 structure–property relationships are randomly divided into two groups: 750 for training and 250 for validation.

The DNN architecture (i.e. the combination of DNN layers) was modified through parameter tuning during the training process to obtain a satisfactory accuracy and learning rate. MSE (mean squared error) is adopted to train the model and optimize the parameters. The definition of MSE is presented in Equation (11) below:

$$MSE_{(y_{true},y_{pred})} = (y_{true} - y_{pred})^2 \tag{11}$$

where y_{true} is the ground truth of the stress property from CPFE modelling results, and y_{pred} is the predicted value by DNN, and L is the MSE loss function.

The DNN architecture can be summarized in the formula below:

$$y_{pred} = \varnothing^L(\theta^L, \varnothing^{L-1}(\theta^{L-1}\cdots\varnothing^1(\theta^1, x)\cdots)) \tag{12}$$

where x is the input into this model, θ^L is the L^{th} layer's parameters (note that there may be more than 1 parameter existing in a neural network layer, but they are all represented by a single θ here), and $\varnothing^L$ means the activation function and layer type of the L^{th} layer.

Hence, the loss function can be rewritten as:

$$\begin{aligned} &L(y_{true}, \varnothing^L(\theta^L, \varnothing^{L-1}(\theta^{L-1}\cdots\varnothing^1(\theta^1, x)\cdots))) \\ &= abs(y_{true} - \varnothing^L(\theta^L, \varnothing^{L-1}(\theta^{L-1}\cdots\varnothing^1(\theta^1, x)\cdots))) \end{aligned} \tag{13}$$

Therefore, for each θ, it is possible to compute its gradient with a chain rule. This back propagation (BP) algorithm was adopted for the training of the DNN [71]. For example, considering θ^1 the gradient is:

$$\frac{dL}{d\theta^1} = \frac{dL}{d\varnothing^L}\frac{d\varnothing^L}{d\varnothing^{L-1}}\cdots\frac{d\varnothing^1}{d\theta^1} \tag{14}$$

After getting the gradient of parameter θ, it is updated as:

$$\theta' = \theta - \alpha\frac{dL}{d\theta} \tag{15}$$

where α is referred to as a learning rate.

The Keras library and the efficient implementation of BP (SGD) were adopted in this optimization process [78].

Table 2
Relationship between DNN performance and the training/validation ratio setting.

Training/validation ratio	MAE in YS (MPa)
50–50	332.0
60–40	317.8
70–30	45.3
75–25	37.1
80–20	38.6

The remaining unseen unique 250 sets of CPFE predicted structure–property relationships are used to validate the reliability of the trained DNN model. Two criteria, MAE and regression residual are used for determining the DNN model performance in both efficiency and accuracy. MAE quantifies the error between the predicted values and ground truth of the 250 data points. The regression residual is computed as $|y_{true} - y_{pred}|/y_{true}$ and reported in percentage terms.

2.5. DNN validation with new phase fraction dataset

The effectiveness of the DNN model predictive capability for other phase fraction combinations was then assessed. Thus, 200 more synthetic microstructure images were generated for two martensite fractions ($V_{f,m}$ = 35%, 65%) that are between previous fraction values (5, 20, 50, 80, 95%). In this case, no re-training of the DNN model was performed; however, CPFE analyses were performed for validation of the predicted yield strength.

2.6. DNN application on realistic microstructural images

CPFE modelling based directly on realistic microstructure images, (based on SEM or EBSD scans) is considered to more accurately represent microstructure with complex grain morphologies and special textures common in AM metals, [19,21,79,80] than using synthetic (e.g. VT-based) images. However, this real image-based model usually has higher computational cost and larger computational memory requirements [81]. Furthermore, time-consuming sample preparation and pre-processing of the raw data, including non-indexed fill and grain cleaning, is necessary to avoid excessive numbers of local singularities.

The DNN model is potentially capable of addressing the excessive computational cost issue associated with solving EBSD-CPFE models. To test this capability, a 400×400 pixel EBSD scan of 17-4PH material was performed. The EBSD images were converted to a phase image together with an IPF coloured orientation map (for texture data) with which the trained DNN is familiar. Meanwhile, an EBSD image-based CPFE model was constructed using a previously published approach [19]. To distinguish from the VT-generated CPFE model, all models from direct EBSD image-based conversion are subsequently denoted as CPFE-E. The DNN and CPFE-E predicted stress–strain curves using realistic microstructural images were compared to the experimental test to determine predictive accuracy. The computational costs were also measured to compare efficiency.

3. Results

3.1. CPFE model calibration and property prediction

This study started with CPFE model calibration against the mechanical tests. Fig. 5 shows a statistically equivalent RVE model (21% austenite phase and equivalent texture), based on microstructural characterization from EBSD measurement, for this parameter calibration process. Fig. 6 shows a comparison between CPFE-predicted and measured experimental tensile stress–strain response. This CPFE model shows close agreement up to the strain of 1%, including good agreement of yield stress (1066 and 1087 MPa).

The next step was to validate the performance for steels with different phase fractions. For ease of results visualization and comparison, Fig. 7 shows the 0.2% offset yield stress (YS) values extracted from the 1000 CPFE models with five different phase fractions. The CPFE model predicted an increasing tensile strength as the martensite fraction increases with the predicted YS median

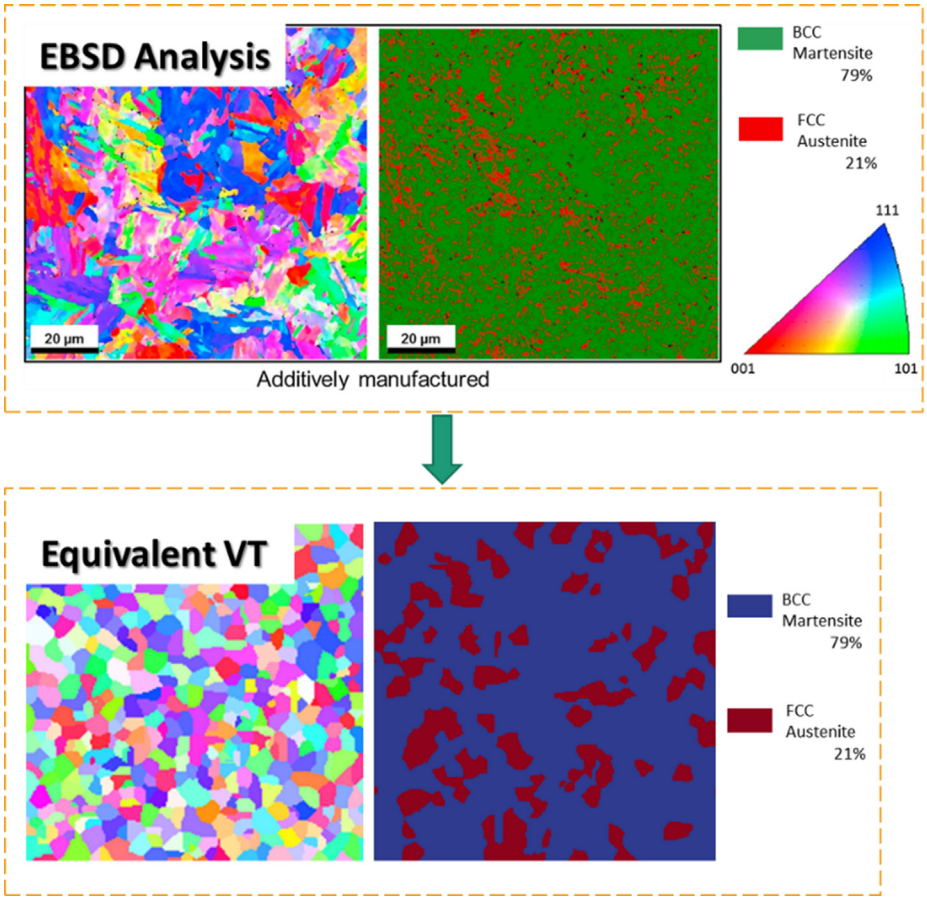

Fig. 5. Reconstructed EBSD crystallographic orientation map coloured in inverse pole figure (IPF), phase fraction map (79% martensite in green and 21% austenite in red), and the statistically equivalent VT-generated CPFE model.

values being 532 MPa, 567 MPa, 702 MPa, 1003 MPa and 1216 MPa for the groups with 5, 20, 50, 80, 95% martensite phase, respectively. The CPFE-predicted YS ranges are also compared with tensile test data for other AM steels for a range of martensite phase fractions in Table 3.

Fig. 8 shows the CPFE-predicted stabilized hysteresis stress–strain loop relationship at three strain amplitudes, ±0.4%, ±0.7%, and ± 1.0%. FCI is assumed to correspond to a critical FIP W value, which is calibrated against the ± 1.0% CPFE result as

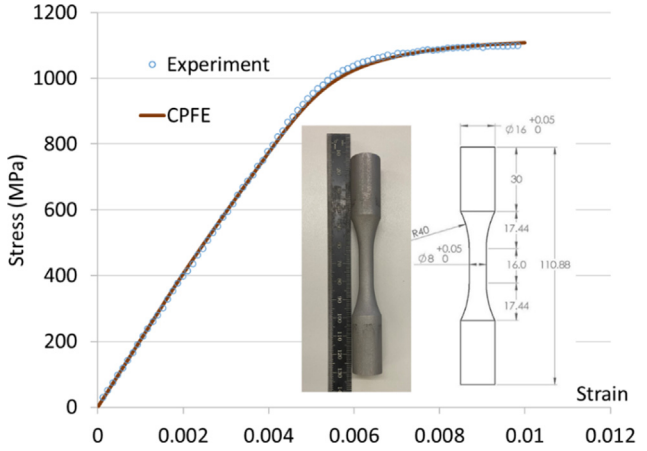

Fig. 6. Experimental fit and CPFE parameters calibration for SLM manufactured 17-4PH steel.

$8.26 \times 10^5 MJm^{-3}$. The maximum localized FIP W is adopted to indicate the predicted FCI life. Table 4 shows a comparison between predicted and measured stress amplitudes and FCI lives. Both FIPs show a decreasing trend until they finally become stable after 8 cycles. The FIP energy dissipation W result from the tensile test simulation can, to some extent, represent the cyclic FIP result by multiplying it by a factor of four while the plastic slip p result shows overestimation when predicting maximum localization values. A previous study [58] also showed a more reliable prediction on fatigue behaviour using W rather than p. Due to the above reasons, this work only considers energy dissipation W values as the FIP and uses tensile CPFE modelling results for the DNN training to save computational cost.

Fig. 9 shows the 1000 maximum localized FIP W distribution results extracted from big data CPFE models. It can be observed that for a group of randomly generated models with a constant phase fraction definition but unique morphology and texture, there is approximately a 3% possibility for the CPFE models to predict double the localized FIP values compared to the mean FIP of the phase group. The CPFE models have predicted a wide range of FIPs although their phase compositions are statistically equivalent. One reason is the difference in RVE size for a monotonic stress–strain prediction and the RVE size for maximum FIP value prediction. The RVE size used here meets the requirements for monotonic stress–strain but may not suffice for some model FIP predictions. It is known that the predicted fatigue life reduces as the RVE size increases [19]; however model size in this work (of 1000 CPFE models) had to be balanced with computational costs of the CPFE analysis. In addition, the FIP prediction has proved to be more sen-

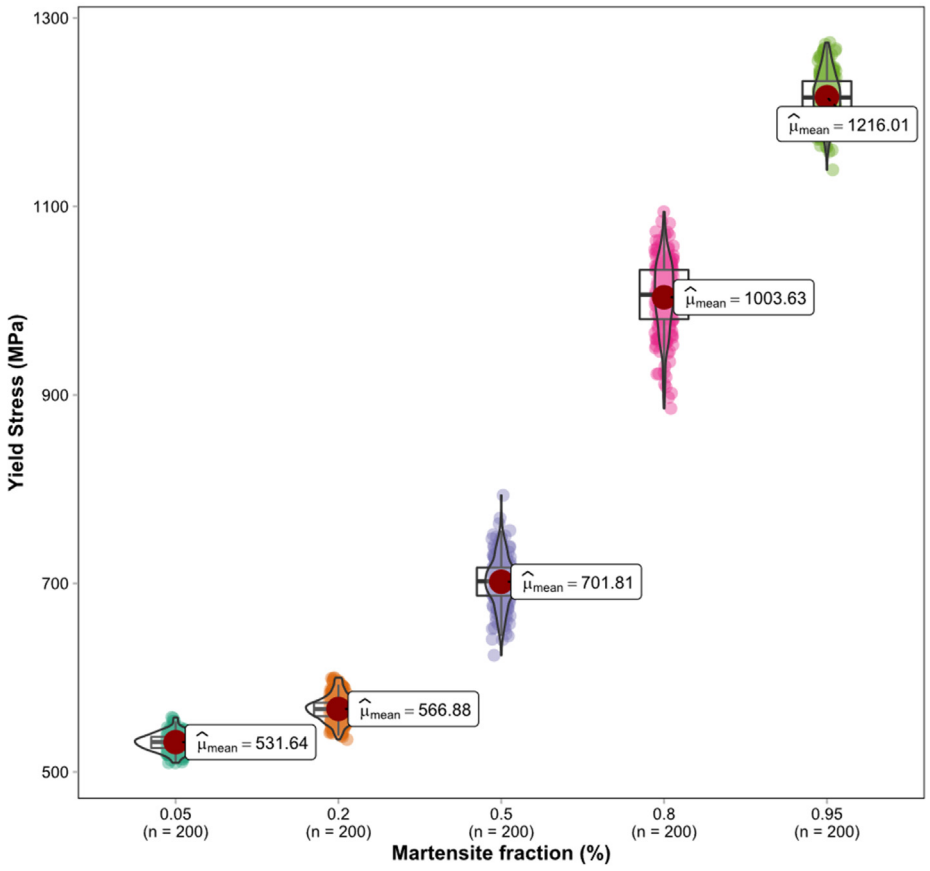

Fig. 7. CPFE predicted effect of martensite phase fraction on yield stress.

Table 3
Comparison of CPFE predicted results with literature on yield strength.

Martensite Fraction (%)	CPFE YS ranges (MPa)	Test YS (MPa)
5	509.7–557.9	440–520 [82–84]
20	534.4–600.0	570 [85]
50	623.8–793.5	750–798 [34,86]
80	824.9–1094.3	1087 [33]
95	1138.8–1270.0	1170 [30]

sitive to the initial texture than to grain morphology. The texture is randomly assigned to the models within the same phase group and is unique in individual RVEs. In each phase group, there are approximately 5 FIP predictions considerably higher than the mean. It is worth noting that although a bigger RVE decreases the possibility of large scatter in the FIP prediction, it is unlikely to account for all scatter [87]. Fig. 10 shows von Mises stress, principal strain, and FIP *W* contour plots for phase fractions of 20% and 80% at the strain of 1%. The 80% martensite material gives a higher von Mises stress and fewer deformed regions due to increased harder phase components. The FIP *W* shows a similar distribution to the principal strain contour plot, while its magnitude is influenced by both stress and strain localization values.

3.2. DNN training and validation performance

The hardware requirement for the developed DNN model is low and all DNN code in this work run on an office grade laptop with 4-

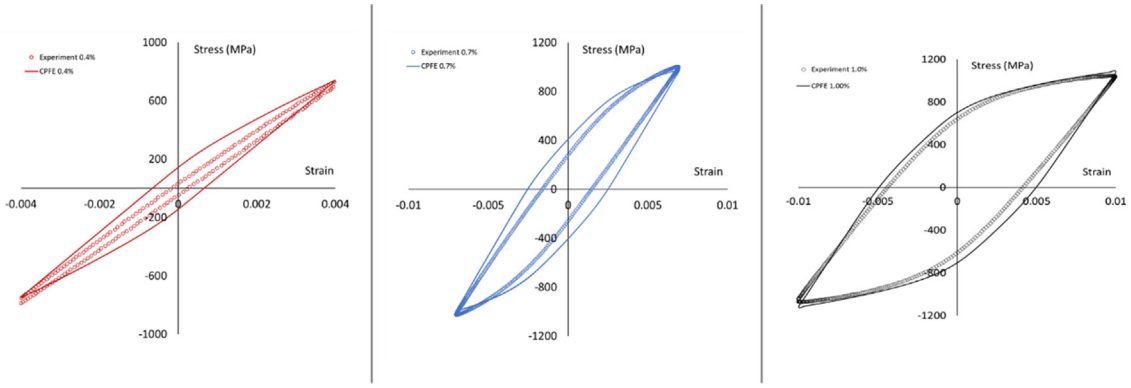

Fig. 8. Comparison of CPFE-predicted stabilized hysteresis loop (lines) with experimental data (symbols), for the 79% martensite phase fraction in 17-4PH AM steel, at 0.4%, 0.7% and 1.0% cyclic strain amplitudes.

Table 4
Comparison between experimental tests and CPFE predicted results on cyclic stress and fatigue crack initiation life.

Strain amplitude	Experiment $\Delta\sigma/2$	CPFE $\Delta\sigma/2$	N_i Test (cycles)	N_i CPFE (cycles)
±0.4%	792 MPa	748 MPa	11,271	11,399
±0.5%	921 MPa	862 MPa	4011	3352
±0.7%	1014 MPa	994 MPa	633	956
±1.0%	1060 MPa	1108 MPa	129	125

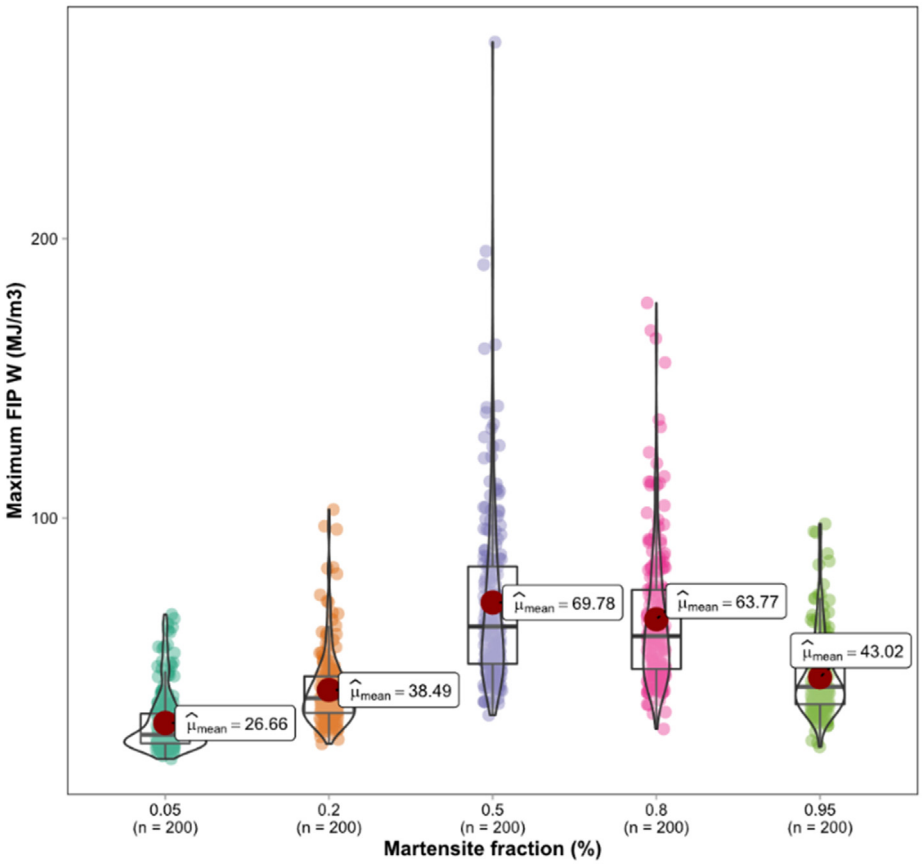

Fig. 9. Predicted effect of martensite phase fractions on the maximum localized energy dissipation FIP *W* over full RVE extracted from CPFE models.

core CPU and 16 GB RAM. The design and arrangement of DNN layers has a significant impact on training time and convergence values, but not on the convergence speed. The optimised non-sequence DNN model in Fig. 4 (b), with 2 input layers and 3 CNN layers for each branch, had an accuracy of 91% (compared to the standard sequence DNN model of 65%) but required a larger training time of 25 min (compared to 15 min).

Fig. 11 compares the training loss and validation loss curves for the standard sequence DNN (a) and the advanced non-sequence DNN after model optimization (b). From these two figures, it can be concluded that after optimization, the latter model creates far better predictions with significantly reduced MAE. The MAE curve for the model before optimization fails to converge, as shown in Fig. 11 that after 25 epochs the validation loss is still not steady. After improving the DNN to non-sequence multi-pipeline type, the loss curves begin to converge after 20 epochs, giving a more robust model. To further distinguish the two DNN model types, Fig. 12 plots the regression residual for the two network structures. Similar to the conclusion drawn by MAE, after optimization, the mean of regression residual has decreased, indicating that the model can perform more accurate prediction and the variance of the regression residual has also decreased indicating that the optimized model is less likely to produce outliers. Table 5 and Table 6 list the structural parameters of the two models before and after optimization. Although the optimized model adds more parameters in total which may lead to slightly more training time, it results in largely improved performance. Thus, all DNN models hereafter in this study employ the optimized non-sequence structure.

It takes 3 s for the DNN to give stress–strain relationships for all 250 models in the validation group, while it takes 4 days to complete CPFE modelling of the equivalent data set. Fig. 13 show the stress–strain curve comparison from two randomly picked models in the 250 validation group of 80% martensite phase fraction. Fig. 14 plots the comparison between 0.2% offset yield strength predicted by CPFE modelling and DNN machine learning, including both training and validation groups. The validation group tends to overpredict the YS value for the 50% phase fraction group, but the general predicting error is controlled within ±15% margin.

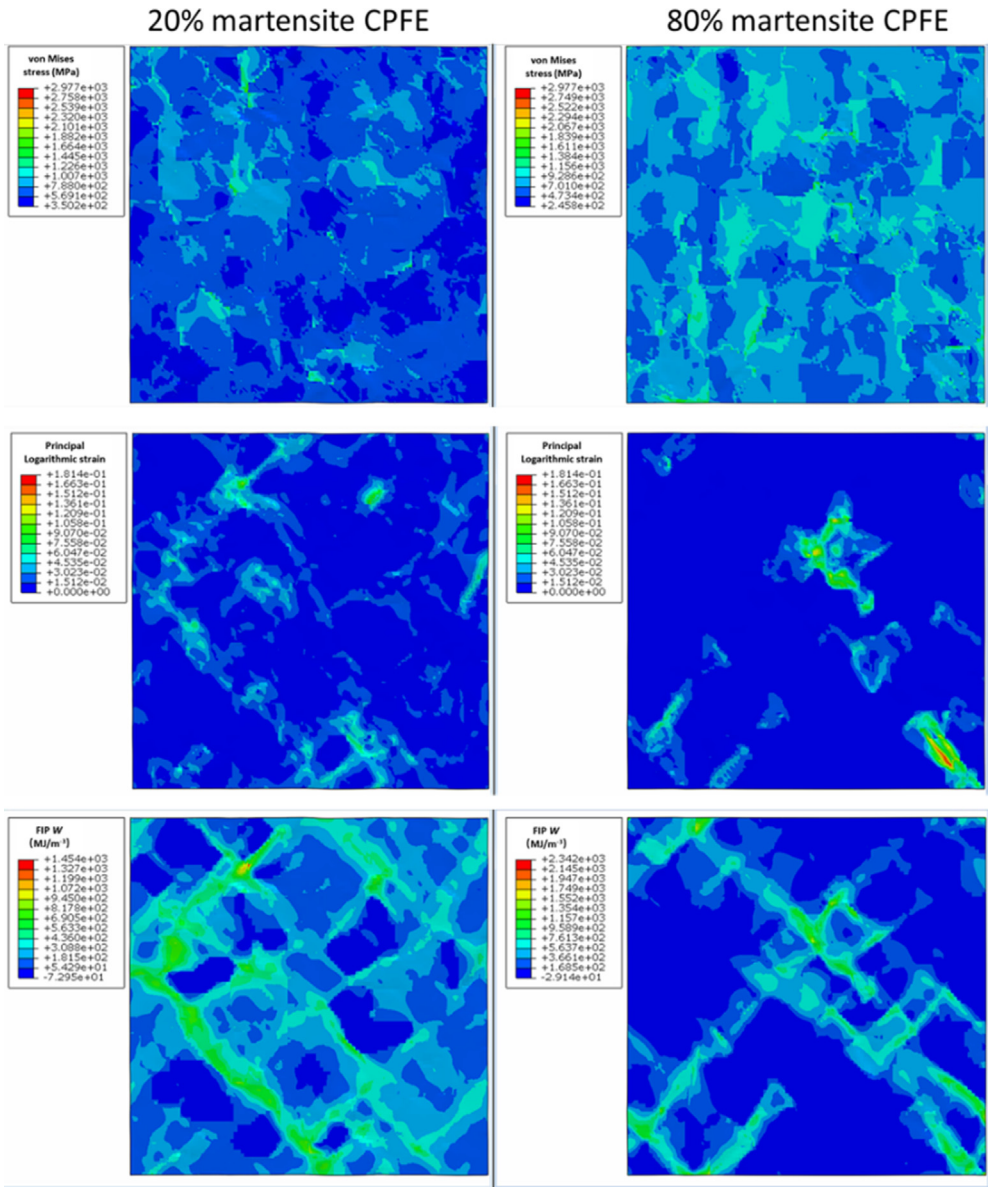

Fig. 10. Predicted effect of martensite phase fraction on CPFE-predicted distribution of von-Mises stress, maximum principal strain and *W* FIP.

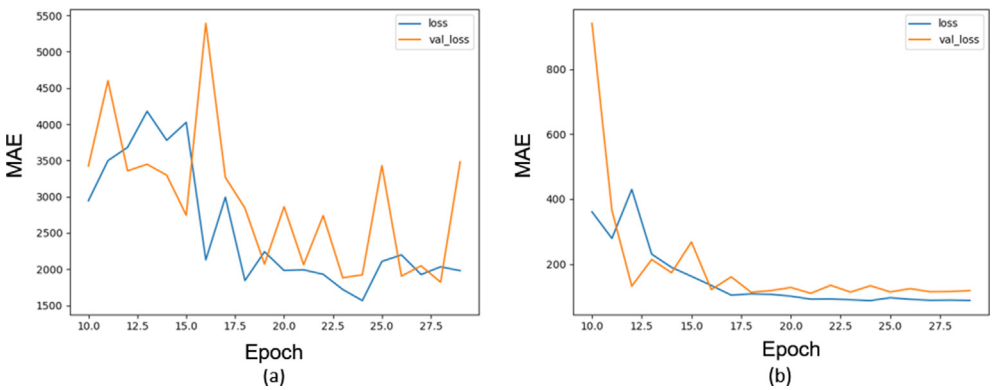

Fig. 11. MAE loss curves (loss for training group and val_loss for validation group) of the DNN network (a) before and (b) after optimization.

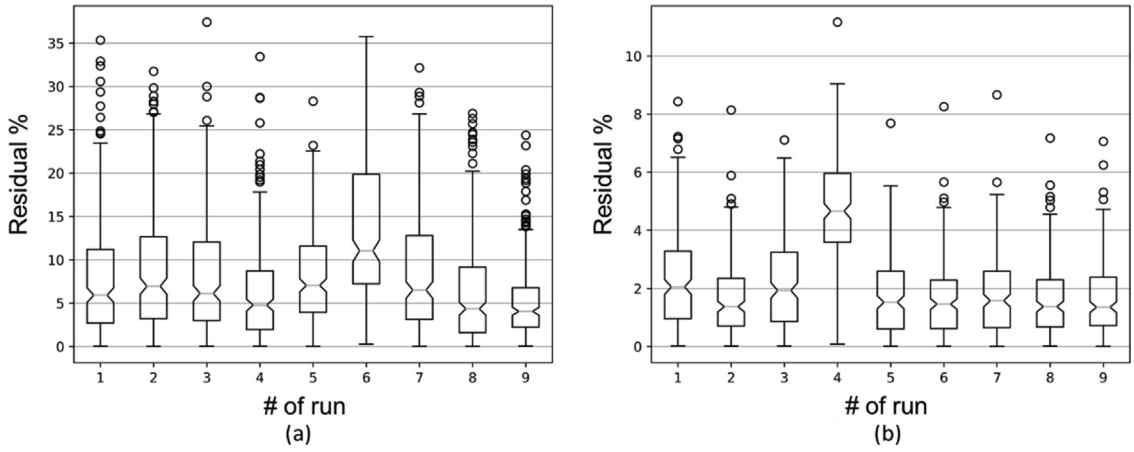

Fig. 12. Regression residual (residual %) boxplot of the DNN network performance (a) before and (b) after optimization.

Table 5
Standard DNN structure design parameters before optimization.

Layer (type)	Output Shape	Param #
Conv2D	(BATCH, 98, 98, 32)	896
MaxPooling2D	(BATCH, 49, 49, 32)	0
Conv2D	(BATCH, 47, 47, 64)	18,496
MaxPooling2D	(BATCH, 23, 23, 64)	0
Conv2D	(BATCH, 21, 21, 64)	36,928
Flatten	(BATCH, 28224)	0
Dense	(BATCH, 64)	1,806,400
Dense	(BATCH, 1)	65
Total		1,862,785

Table 6
Non-sequence (Siamese) DNN structure design parameters after optimization.

Layer (type)	Output Shape	Param #
Conv2D	(BATCH, 98, 98, 32)	896
MaxPooling2D	(BATCH, 49, 49, 32)	0
Conv2D	(BATCH, 47, 47, 64)	18,496
MaxPooling2D	(BATCH, 23, 23, 64)	0
Conv2D	(BATCH, 21, 21, 64)	36,928
Flatten	(BATCH, 28224)	0
Dense	(BATCH, 32)	903,200
Conv2D	(BATCH, 98, 98, 32)	896
MaxPooling2D	(BATCH, 49, 49, 32)	0
Conv2D	(BATCH, 47, 47, 64)	18,496
MaxPooling2D	(BATCH, 23, 23, 64)	0
Conv2D	(BATCH, 21, 21, 64)	36,928
Flatten	(BATCH, 28224)	0
Dense	(BATCH, 32)	903,200
Concatenate	(BATCH, 64)	0
Dense	(BATCH, 64)	1040
Dense	(BATCH, 1)	17
Total		1,920,097

Fig. 15 shows the CPFE and DNN predicted contour plots of von Mises stress (CPFE) and heat-map (weight factor) for contributing pixels (DNN) at 1% strain for 20%, 50% and 80% martensite fraction models, respectively. The contour plots on the left side are directly from CPFE modelling showing von Mises stress, while the contour plots on the right side are the weight factor distribution extracted from the DNN convolutional layer to the overall stress–strain response. It should be noted that the DNN model is not designed to predict the von Mises stress contour plot, but these images are presented to indicate the relative contribution that each grain makes to the DNN response prediction. The weight factor heatmap shows the correlation of microstructural images to the stress property after DNN training, where the red regions contribute most to the overall stress (DNN output property) while the blue regions have the least positive effect on the property. It is obvious that the black phase (martensite) has the higher weight factor leading to a higher stress localization, which is consistent with the CPFE model prediction because martensite is defined to be harder. Fig. 16 shows a similar comparison between the CPFE contour plot of FIP W and the corresponding DNN predicted heat map for FIP W. The CNN weight factor heatmap reveals what the DNN model has interpreted. The comparison between the heatmap and the relevant physical-based CPFE model stress contour plot, helps assess and improve the DNN performance. Besides, the localized mechanical property prediction, rather than a macroscopic stress–strain curve, offers a more visible and straightforward reference for tailored microstructure design or localized quality assessment.

3.3. DNN structure–property prediction on customized multiphase steels.

The developed DNN tool was adopted for predicting the YS values out of the newly generated 400 models with 35% and 65% martensite fractions, respectively. CPFE modelling result with the same phase fraction was only adopted for validating the DNN predictions. Fig. 17 shows a randomly selected example from the 200 models and compares the predicted stress localization contour plots. Together with the previous 1000 models for DNN training and validation, Fig. 18 shows the DNN predicted structure–property relationship curve defined by YS and phase fraction including 7 phases totally. The averaged YS values from the two selected CPFE models in Fig. 17 were plotted (in black diamonds) to validate the two new phase DNN predictions. A third order polynomial equation was implemented here to quantify the trend relationship as $YS = f(V_{f,m})$, which shows a similar trend compared to the hardness testing data for similar materials in the literature [88].

3.4. DNN structure–property prediction on a realistic EBSD scan.

Fig. 19 (a) shows the EBSD data and images containing phase and orientation information as the DNN input. The realistic EBSD image has 321,602 pixels, equal to the number of nodes required in the converted CPFE-E model. The reconstructed EBSD map with 24,406 grains is meshed with C3D8 hexagonal voxels as shown in

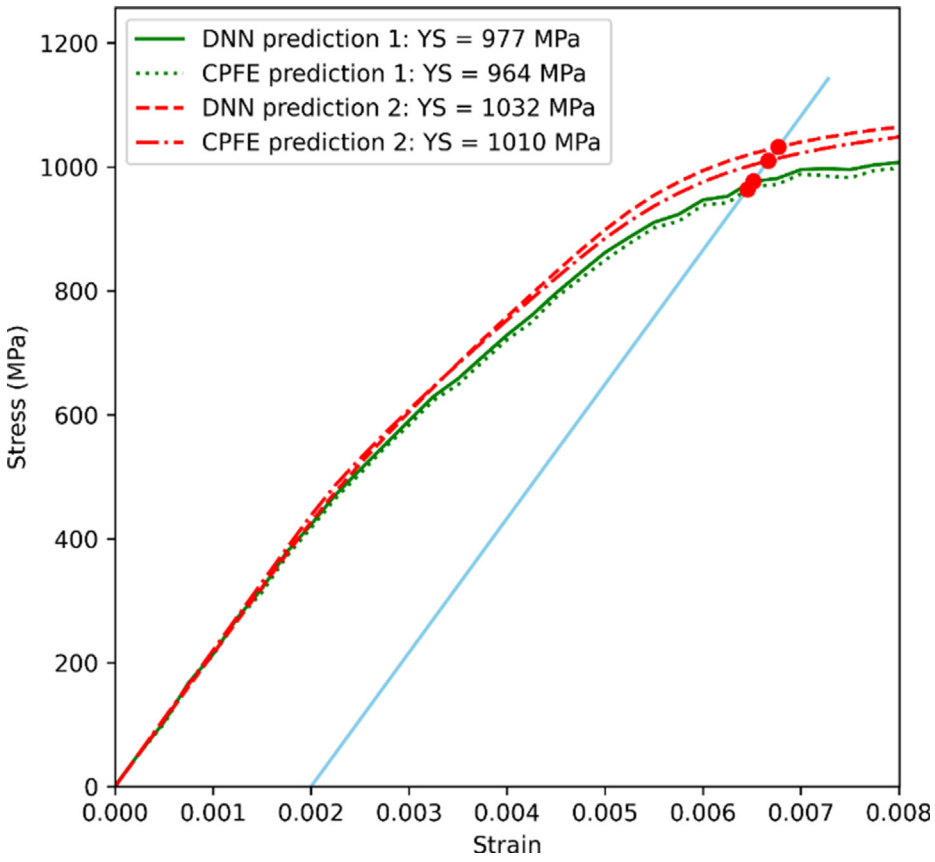

Fig. 13. Comparison between CPFE- and DNN-predicted tensile stress–strain response up to 0.8% strain for 80% phase fraction of martensite.

Fig. 19 (b). One key benefit of the DNN model is again the much higher computational efficiency. It takes 45 min for the customized code to generate the necessary CPFE-E input file. It takes 13 h to finish the real image-based CPFE-E modelling due to the model size and higher resolution. Yet it only takes 1.27 s for the trained DNN tool to output the stress prediction and most of that time is consumed with data transfer.

Fig. 20 shows the stress–strain curve comparison between CPFE-E, DNN prediction and the experiment test. The YS prediction from CPFE-E and DNN are 1049 MPa and 1095 MPa respectively, compared to the experimentally obtained 1087 MPa. The DNN predicted stress–strain behaviour after yield is slightly closer to the experimental test in this case. In this case, the higher predicted stress from CPFE-E might be due to the small size of some austenite grains and could be solved using a higher resolution. However, this solution further increases the computational cost. In this real image based study, while both CPFE-E and DNN models successfully predict stress–strain curves, the developed DNN model has shown higher efficiency and accuracy when predicting mechanical properties, albeit with a non-smooth computational stress–strain curve.

4. Discussion

This study has presented a CPFE trained DNN tool with the ability to predict mechanical response based on microstructural images. In CPFE, the phase and orientation data determine the individual grain properties in microscale finite element based modelling of grain deformation and interaction under a given loading condition. Within the DNN tool (trained from prior CPFE analyses), microstructural detail such as phase and orientation are regarded as a combination of pixels with different weight factors for the prediction. Every pixel in the image contributes to the prediction depending on this weight factor, and together they determine the mechanical response metrics. The predicted contour plots and heat maps are shown in Fig. 15 and Fig. 16 to demonstrate this principle. Both CPFE contour plots represent the localised mechanical response while the hottest region in the DNN heatmap represents the pixels with the most significant influence (high weight factor) on the DNN predicted mechanical property. From these contours, the DNN successfully captures the stress localization at similar hot spots to the CPFE results. The difficulty lies around the grain boundary when DNN knows to assign different weight factors on the grain boundary curves but fails to always find the correct trends. Precise grain boundary modelling is also a challenge for CPFE modelling. The consistent fit between stress distribution maps explains the satisfying prediction of stress–strain behaviour and yield strength. Moreover, it can be deduced that the integrated CPFE-DNN tool developed in this paper has the potential to predict hysteresis loops by extending current CPFE tensile models to fatigue, without the need to change the DNN model architecture.

When it comes to FIP prediction, see Fig. 21, the MAE curve fails to converge, even with sufficient training iterations (200 epochs), using the same optimized DNN model. Fig. 16 visually shows how the DNN model fails to identify the dominant grains for FIP W contribution (per the CPFE result). FIP is an extremely localized value for predicting strong mechanical behaviour such as crack initiation. Thus, fewer clues exist in the training data for the DNN which causes the reduced predictive accuracy. This is in contrast to Fig. 15, where most pixels in the structural input image appropriately contribute to a weight factor when determining bulk tensile stress–strain behaviour as well as the stress localization distribution, resulting in accurate stress–strain prediction.

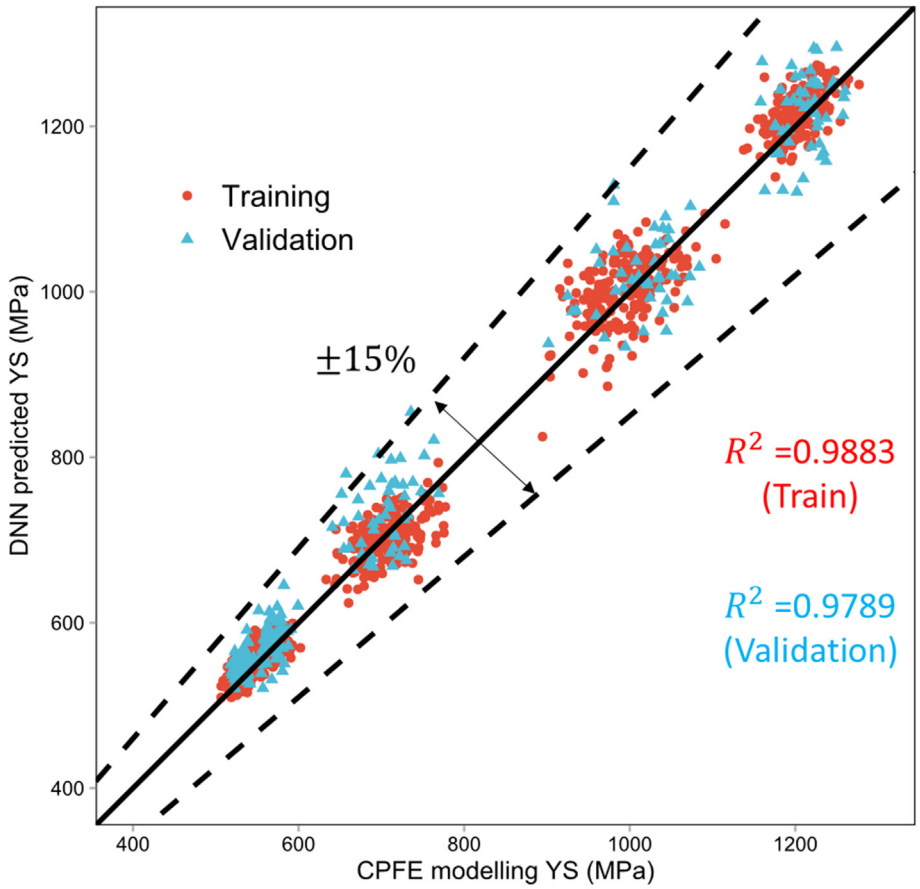

Fig. 14. Comparison between CPFE and DNN (optimized) predicted yield stress values in the training (red) and validation (blue) group. (For interpretation of the references to colour in this figure legend, the reader is referred to the web version of this article.)

DNN architecture optimization has a significant effect on the predicting accuracy in this work. Despite the different settings of the standard and Siamese DNN, they are quite similar in layers and depth. However, the latter achieved lower MAE and regression residual as shown in Figs. 11 and 12, which indicate a better capacity in prediction. The reasons for the results are as follows. (1) The Siamese DNN separates the microstructure inputs Phase and IPF data into two separate pipelines, which enables the model to capture their individual characteristics in different ways without interference. (2) The two different characteristics are merged in the last 3 layers, which guarantees that the model can also capture the common points between Phase and IPF data during the BP algorithm. (3) The Siamese DNN has more parameters compared to the standard type, providing better capability in fitting and predicting the more complex CPFE data.

The two results introduced in Sections 3.3 and 3.4 broaden the practical applications of the developed DNN tool. DNN successfully predicts the structure–property relationship of two new customized phase fraction dual phase steels, even though the DNN model was not specifically trained on that phase fraction or data (EBSD) type. This indicates strong potential for such tools to read in geometrically gradient microstructure images, e.g. growing martensite fraction along built direction and predict the changing property from layer to layer. If the DNN model is designed for the purpose of predicting gradient or flexible phase composition, the phase fraction in training data can be specified to be continuous within the desired range, rather than the discrete values, to further improve the predicting accuracy. The developed DNN model has the ability to predict the structure–property relationships for a real image within milliseconds, providing a rapid non-destructive tensile testing solution once integrated with a high speed in-situ cameras providing live microstructure imaging of a solidified layer. This potential application offers a step towards an instant / real-time determination of tensile mechanical performance based on live process quality control data, for example, the next generation of PBF machines could give a live read-out of the tensile strength of the layer which has just solidified. It is noted that such in-process microstructural imaging captures as-solidified microstructure and so future code surrogates could be expanded to include microstructural evolution predictive steps to account for changes that may occur during cooling or subsequent post-build heat-treatment. In addition, this DNN tool could be expanded to include PBF process-structure modelling capability [89,90], to give a complete process-structure–property instant predictive capability based on selected process parameters and CAD layer/slice data. Further uptake of the developed CPFE-DNN method could be via a non-destructive inspection tool which gives quick and accurate reports on void and microstructural defect characterization, to accompany the existing microscopy techniques.

Furthermore, this model could be reversed to assist microstructure design (determining required microstructural features) for a desired strength response, or use in decision making on the powder mixture ratio for a desired functional gradient material product. The CPFE-DNN method presented can also be easily extended to multiple-phase materials with other chemical compositions.

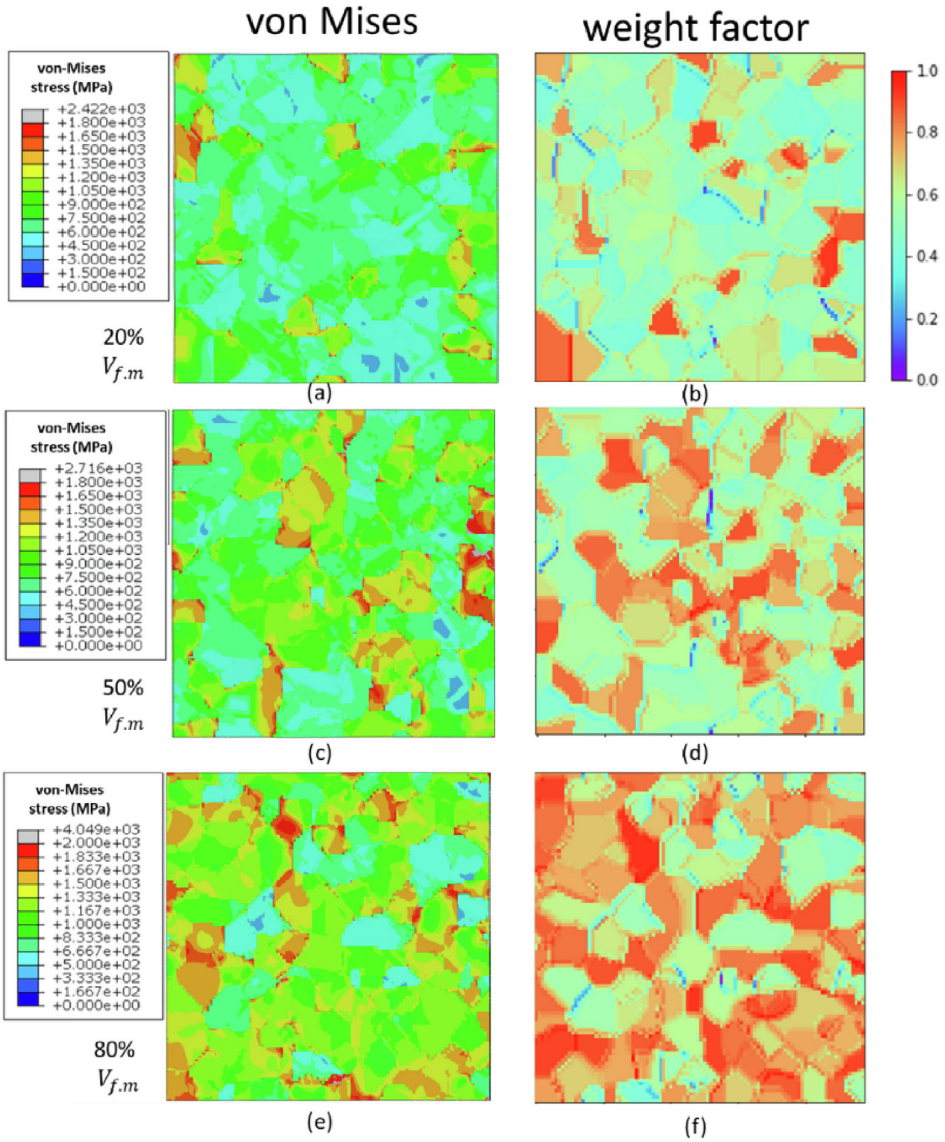

Fig. 15. Effect of martensite phase fraction on CPFE-predicted von Mises stress distribution (left) and corresponding weight factors for CNN layer (right).

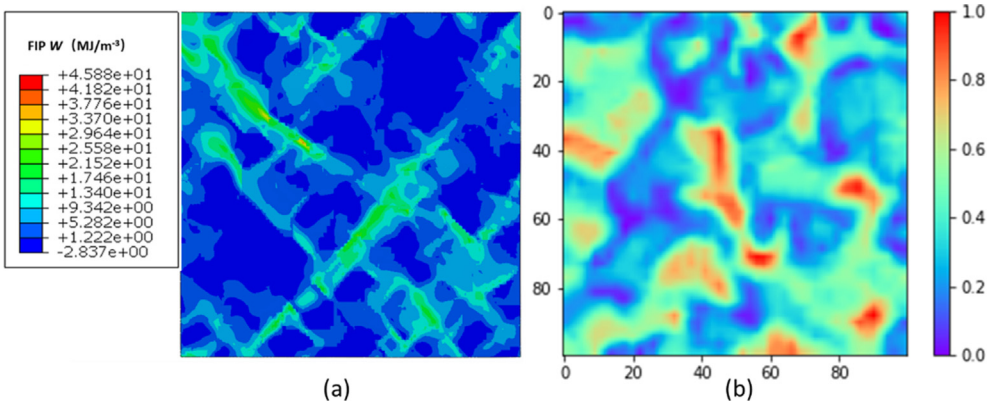

Fig. 16. A comparison of the predicted FIP *W* contour plot from (a) CPFE modelling and (b) CNN layer weight factor.

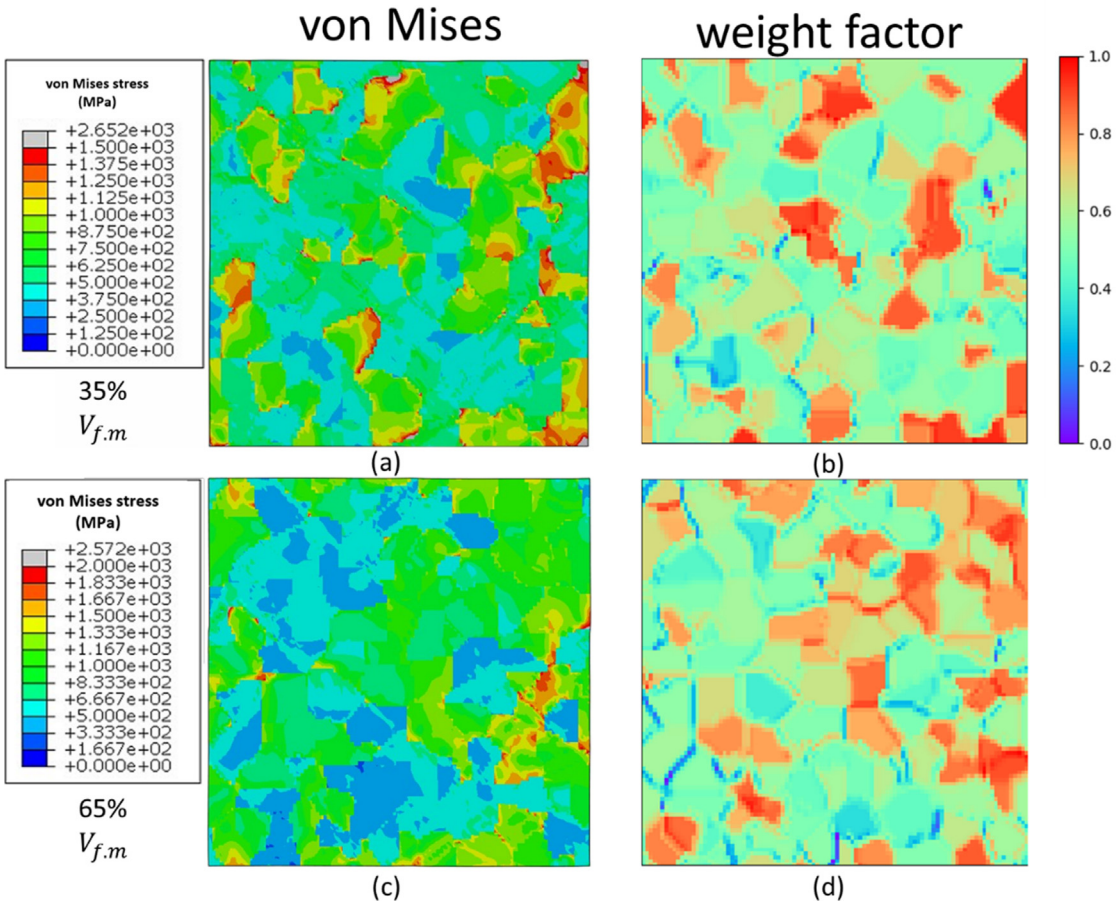

Fig. 17. CPFE and DNN predicted contour plot comparison. 35% martensite phase fraction model: (a) CPFE predicted von-Mises stress distribution and (b) CNN layer weight factor predicted from DNN model. 65% martensite phase fraction model: (c) CPFE predicted von-Mises stress and (d) DNN model weight factor.

5. Conclusions

The Deep Learning model presented here demonstrates one future option for an instant non-destructive property predicting tool, trained by crystal plasticity finite element analysis of microstructure-property relationship and experimental testing. The near-instant strength prediction performance makes it feasible to implement this DL model as a surrogate tool of CPFE and other computationally expensive models, to give rapid prediction of additive manufacturing part performance within a process-monitoring quality control tool. The dual-phase crystal plasticity and DNN models have been developed for relating microstructural features and mechanical response including tensile stress–strain and fatigue indicator parameter behaviour. The CPFE study was scripted and automated for big data generation and an optimized DNN model was implemented with the automated CPFE for data-driven model training. The key conclusions for this research are:

(1) It is viable to develop and train a CPFE-DNN model to successfully predict the stress–strain curve and yield strength to within ±15% error.
(2) The DNN model, while predicting the structure–property relationship as viable alternative tool for CPFE, enables significant computational cost savings (once trained). (The DNN takes 12 ms for VT generated 100-grain predictions and 1.27 s for real EBSD image converted 24406-grain predictions compared to 25 mins and 13 h, respectively, when using full CPFE modelling.)
(3) A data-driven DNN model requires a large number of CPFE predicted samples for training, with 75:25 training:validation ratio recommended. For dual-phase materials, phase fraction and crystallographic texture are sufficient inputs to provide a reliable yield stress for the AM steels.
(4) The design of the DNN hidden layers architecture is important in machine learning parameter optimization. In this case, the prediction accuracy increases from 65% to 91% after improving the sequence DNN to multi-pipeline non-sequence architecture.
(5) It is necessary to run multiple models of the same phase fraction for FIP characterization to account for possible over-prediction of the maximum FIP values.
(6) The DNN model, trained on VT-CPFE data, can identify the main contributing grains to the stress distribution profile, and can accurately predict the tensile stress–strain curve but is less accurate in predicting FIP localization results.
(7) The trained DNN model can be applied to multiple ranges of phase fraction steels, including phase fractions not used in the training data. Most importantly, it is capable of predicting the mechanical response from real EBSD images, despite being trained only on VT models. This is a key step towards a tool for in-situ microstructure-property prediction in real-time.

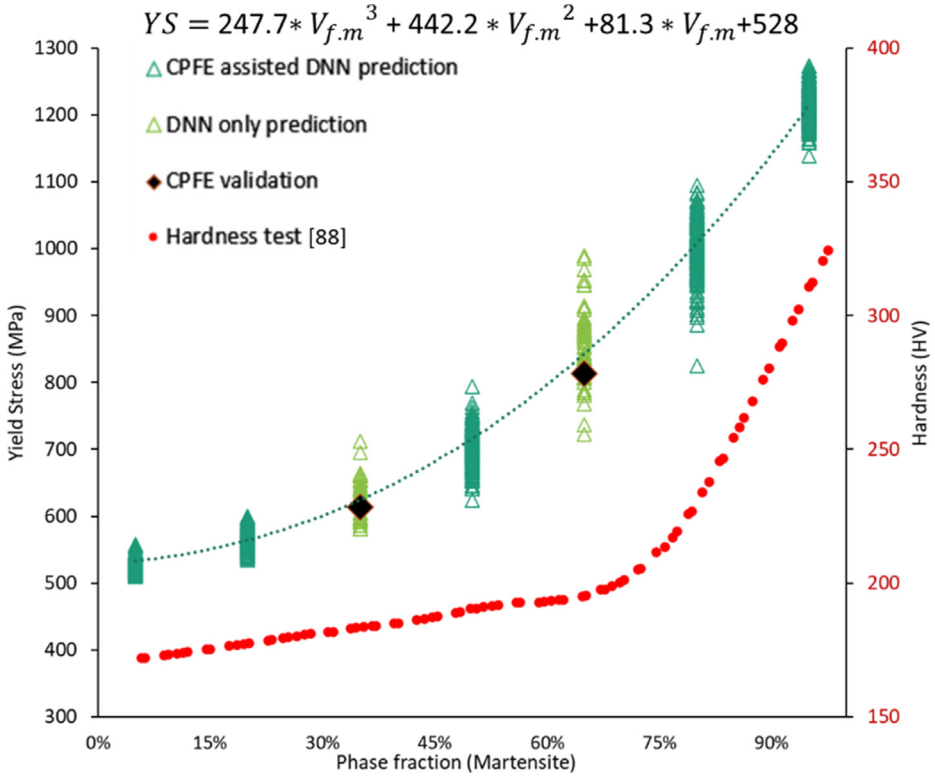

Fig. 18. DNN predicted relationship between martensite phase fraction and yield strength, and comparison with measured effect on hardness.

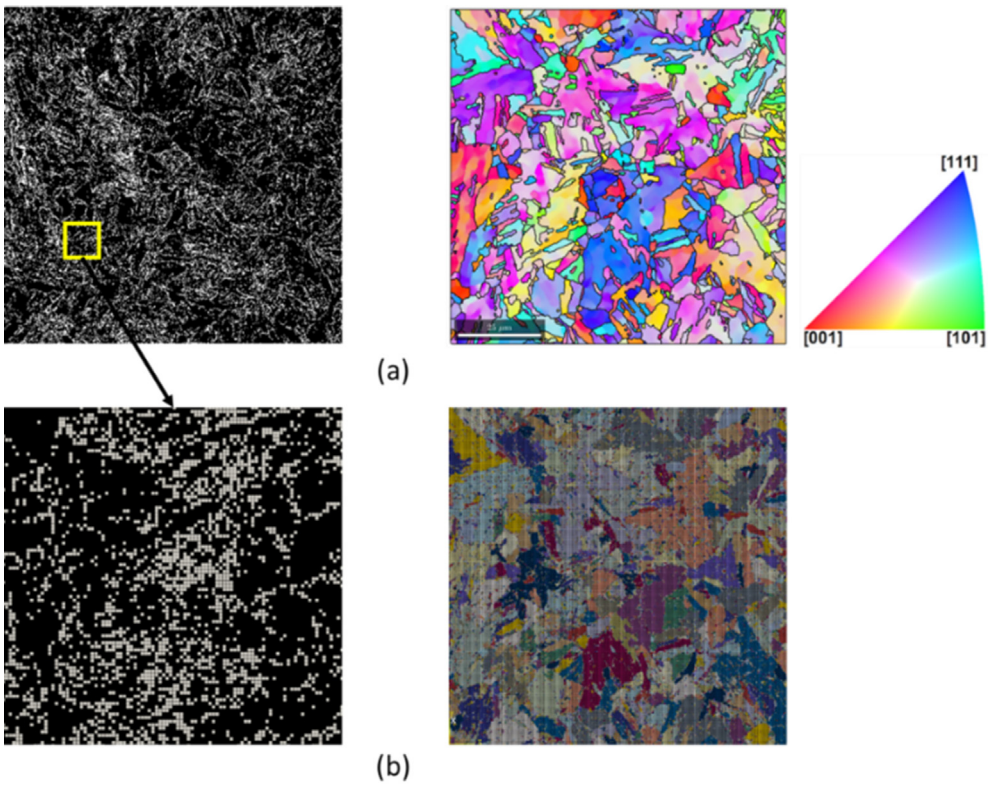

Fig 19. (a) EBSD map data inputs in DNN tool with 321602 pixels: phase composition and IPF coloured crystallographic orientation imaging information. (b) Direct EBSD converted CPFE-E model with 24406 grains using C3D8 hexagonal mesh.

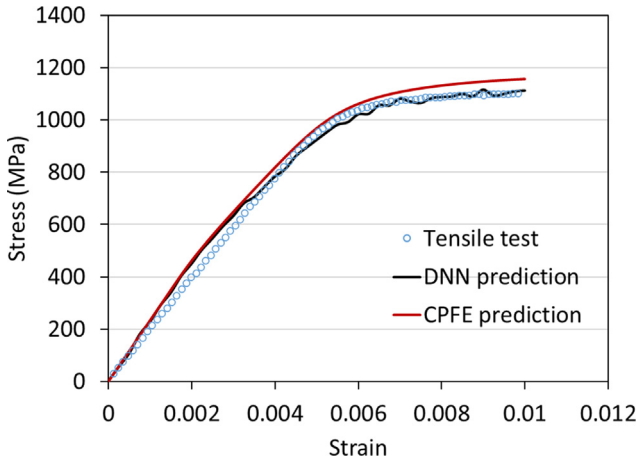

Fig. 20. A comparison of the bulk stress–strain relationship between EBSD image-based DNN model, CPFE-E model and the experimental test.

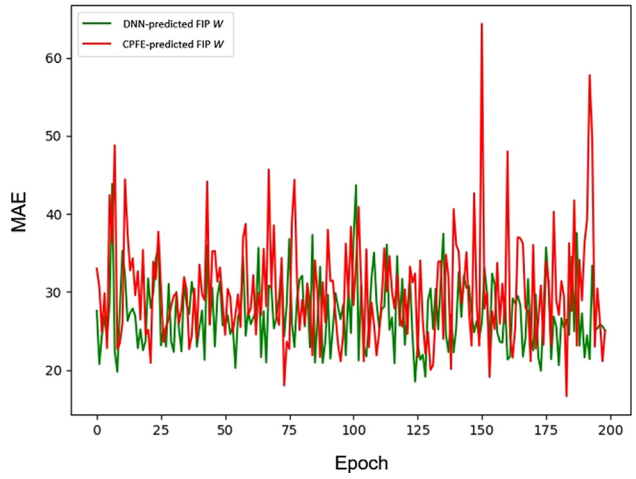

Fig. 21. MAE convergence curve for *W* FIP prediction during DNN training.

Declaration of Competing Interest

The authors declare that they have no known competing financial interests or personal relationships that could have appeared to influence the work reported in this paper.

Acknowledgements

This publication has emanated from research conducted with the financial support of Science Foundation Ireland under Grant number 16/RC/3872. This work acknowledges Prof. Jiang from University of Nevada, Reno for offering EBSD support.

Data Availability

The raw/processed data required to reproduce these findings cannot be shared at this time as the data also forms part of an ongoing study.

References

[1] P. Bajaj, A. Hariharan, A. Kini, P. Kürnsteiner, D. Raabe, E.A. Jägle, Steels in additive manufacturing: A review of their microstructure and properties, Mater. Sci. Eng., A 772 (2020) 138633.
[2] F. Roters, P. Eisenlohr, L. Hantcherli, D.D. Tjahjanto, T.R. Bieler, D. Raabe, Overview of constitutive laws, kinematics, homogenization and multiscale methods in crystal plasticity finite-element modeling: Theory, experiments, applications, Acta Mater. 58 (4) (2010) 1152–1211.
[3] R.J. Asaro, Crystal plasticity, J. Appl. Mech. 50 (4b) (1983) 921–934.
[4] B. Dutta, S. Babu, B. Jared, Chapter 6 - Metal additive manufacturing process modeling and simulation, in: B. Dutta, S. Babu, B. Jared (Eds.), Science, Technology and Applications of Metals in Additive Manufacturing, Elsevier, 2019, pp. 145–191.
[5] M. Lindroos, T. Pinomaa, A. Antikainen, J. Lagerbom, J. Reijonen, T. Lindroos, T. Andersson, A. Laukkanen, Micromechanical modeling approach to single track deformation, phase transformation and residual stress evolution during selective laser melting using crystal plasticity, Addit. Manuf. 38 (2021) 101819.
[6] Y. Geng, N. Harrison, Functionally graded bimodal Ti6Al4V fabricated by powder bed fusion additive manufacturing: Crystal plasticity finite element modelling, Mater. Sci. Eng., A 773 (2020) 138736.
[7] T. Park, L.G. Hector, X. Hu, F. Abu-Farha, M.R. Fellinger, H. Kim, R. Esmaeilpour, F. Pourboghrat, Crystal plasticity modeling of 3rd generation multi-phase AHSS with martensitic transformation, Int. J. Plast. (2019).
[8] A. Cruzado, S. Lucarini, J. Llorca, J. Segurado, Crystal plasticity simulation of the effect grain size on the fatigue behavior of polycrystalline Inconel 718, Int. J. Plast. 113 (2018) 236–245.
[9] C.A. Sweeney, B. O'Brien, FPE. Dunne, P.E McHugh, S.B. Leen, Strain-gradient modelling of grain size effects on fatigue of CoCr stents, Acta Mater. 78 (C) (2014) 341–353.
[10] S. Haouala, S. Lucarini, J. Llorca, J. Segurado, Simulation of the Hall-Petch effect in FCC polycrystals by means of strain gradient crystal plasticity and FFT homogenization, J. Mech. Phys. Solids 134 (2020) 103755.
[11] F. Barbe, L. Decker, D. Jeulin, G. Cailletaud, Intergranular and intragranular behavior of polycrystalline aggregates. Part 1: F.E. model, Int. J. Plast. 17 (4) (2001) 513–536.
[12] F.P.E. Dunne, A. Walker, D. Rugg, A systematic study of hcp crystal orientation and morphology effects in polycrystal deformation and fatigue, Proc. Roy. Soc. A: Math., Phys. Eng. Sci. 463 (2082) (2007) 1467–1489.
[13] L. Li, L. Shen, G. Proust, A texture-based representative volume element crystal plasticity model for predicting Bauschinger effect during cyclic loading, Mater. Sci. Eng., A 608 (2014) 174–183.
[14] R.K. Verma, P. Biswas, T. Kuwabara, K. Chung, Two stage deformation modeling for DP 780 steel sheet using crystal plasticity, Mater. Sci. Eng., A 604 (2014) 98–102.
[15] S. Zarei, R.J. Nedoushan, M. Atapour, The sources of the micro stress and strain inhomogeneity in dual phase steels, Mater. Sci. Eng., A 674 (2016) 384–396.
[16] J. Kadkhodapour, A. Butz, S. Ziaei-Rad, S. Schmauder, A micro mechanical study on failure initiation of dual phase steels under tension using single crystal plasticity model, Int. J. Plast. 27 (7) (2011) 1103–1125.
[17] D.-F. Li, R.A. Barrett, P.E. O'Donoghue, N.P. O'Dowd, S.B. Leen, A multi-scale crystal plasticity model for cyclic plasticity and low-cycle fatigue in a precipitate-strengthened steel at elevated temperature, J. Mech. Phys. Solids 101 (2017) 44–62.
[18] F.P.E. Dunne, D. Rugg, A. Walker, Lengthscale-dependent, elastically anisotropic, physically-based hcp crystal plasticity: Application to cold-dwell fatigue in Ti alloys, Int. J. Plast. 23 (6) (2007) 1061–1083.
[19] Y. Tu, S.B. Leen, N.M. Harrison, A high-fidelity crystal-plasticity finite element methodology for low-cycle fatigue using automatic electron backscatter diffraction scan conversion: Application to hot-rolled cobalt–chromium alloy, Proc. Instit. Mech. Eng., Part L: J. Mater.: Des. Appl. (2021) 14644207211010836.
[20] R. Bandyopadhyay, A.W. Mello, K. Kapoor, M.P. Reinhold, T.F. Broderick, M.D. Sangid, On the crack initiation and heterogeneous deformation of Ti-6Al-4V during high cycle fatigue at high R ratios, J. Mech. Phys. Solids 129 (2019) 61–82.
[21] C.A. Bronkhorst, J.R. Mayeur, V. Livescu, R. Pokharel, D.W. Brown, G.T. Gray, Structural Representation of Additively Manufactured 316L Austenitic Stainless Steel, Int. J. Plast. (2019).
[22] D.-F. Li, R.A. Barrett, P.E. O'Donoghue, C.J. Hyde, N.P. O'Dowd, S.B. Leen, Micromechanical finite element modelling of thermo-mechanical fatigue for P91 steels, Int. J. Fatigue 87 (2016) 192–202.
[23] D. Wilson, W. Wan, F.P.E. Dunne, Microstructurally-sensitive fatigue crack growth in HCP, BCC and FCC polycrystals, J. Mech. Phys. Solids 126 (2019) 204–225.
[24] P.J. Ashton, T.-S. Jun, Z. Zhang, T.B. Britton, A.M. Harte, S.B. Leen, F.P.E. Dunne, The effect of the beta phase on the micromechanical response of dual-phase titanium alloys, 100(P1) (2017).
[25] C.A. Sweeney, W. Vorster, S.B. Leen, E. Sakurada, P.E. McHugh, F.P.E. Dunne, The role of elastic anisotropy, length scale and crystallographic slip in fatigue crack nucleation, J. Mech. Phys. Solids 61 (5) (2013).
[26] S. Lucarini, J. Segurado, An upscaling approach for micromechanics based fatigue: from RVEs to specimens and component life prediction, Int. J. Fract. (2019).
[27] W.E. Frazier, Metal Additive Manufacturing: A Review, J. Mater. Eng. Perform. 23 (6) (2014) 1917–1928.
[28] T.M. Mower, M.J. Long, Mechanical behavior of additive manufactured, powder-bed laser-fused materials, Mater. Sci. Eng., A 651 (2016) 198–213.
[29] H. Irrinki, J.S.D. Jangam, S. Pasebani, S. Badwe, J. Stitzel, K. Kate, O. Gulsoy, S.V. Atre, Effects of particle characteristics on the microstructure and mechanical properties of 17–4 PH stainless steel fabricated by laser-powder bed fusion, Powder Technol. 331 (2018) 192–203.

[30] H.K. Rafi, D. Pal, N. Patil, T.L. Starr, B.E. Stucker, Microstructure and mechanical behavior of 17–4 precipitation hardenable steel processed by selective laser melting, J. Mater. Eng. Perform. 23 (12) (2014) 4421–4428.
[31] Y. Sun, R.J. Hebert, M. Aindow, Effect of heat treatments on microstructural evolution of additively manufactured and wrought 17–4PH stainless steel, Mater. Des. 156 (2018) 429–440.
[32] A. Yadollahi, M. Mahmoudi, A. Elwany, H. Doude, L. Bian, J.C. Newman, Effects of crack orientation and heat treatment on fatigue-crack-growth behavior of AM 17–4 PH stainless steel, Eng. Fract. Mech. 226 (2020) 106874.
[33] L. Carneiro, B. Jalalahmadi, A. Ashtekar, Y. Jiang, Cyclic deformation and fatigue behavior of additively manufactured 17–4 PH stainless steel, Int. J. Fatigue 123 (2019) 22–30.
[34] A. Kudzal, B. McWilliams, C. Hofmeister, F. Kellogg, J. Yu, J. Taggart-Scarff, J. Liang, Effect of scan pattern on the microstructure and mechanical properties of Powder Bed Fusion additive manufactured 17–4 stainless steel, Mater. Des. 133 (2017) 205–215.
[35] K. Benarji, Y. Ravi Kumar, A.N. Jinoop, C.P. Paul, K.S. Bindra, Effect of heat-treatment on the microstructure, mechanical properties and corrosion behaviour of SS 316 structures built by laser directed energy deposition based additive manufacturing, Met. Mater. Int. 27 (3) (2021) 488–499.
[36] X. Chen, J. Li, X. Cheng, H. Wang, Z. Huang, Effect of heat treatment on microstructure, mechanical and corrosion properties of austenitic stainless steel 316L using arc additive manufacturing, Mater. Sci. Eng., A 715 (2018) 307–314.
[37] A. Azarniya, X.G. Colera, M.J. Mirzaali, S. Sovizi, F. Bartolomeu, M.k. St Weglowski, W.W. Wits, C.Y. Yap, J. Ahn, G. Miranda, F.S. Silva, H.R. Madaah Hosseini, S. Ramakrishna, A.A. Zadpoor, Additive manufacturing of Ti–6Al–4V parts through laser metal deposition (LMD): Process, microstructure, and mechanical properties, J. Alloys Compounds 804 (2019) 163–191.
[38] S.L. Lu, H.P. Tang, Y.P. Ning, N. Liu, D.H. StJohn, M. Qian, Microstructure and mechanical properties of long Ti-6Al-4V rods additively manufactured by selective electron beam melting out of a deep powder bed and the effect of subsequent hot isostatic pressing, Metall. Mater. Trans. A 46 (9) (2015) 3824–3834.
[39] S.A. Razavi, F. Ashrafizadeh, S. Fooladi, Prediction of age hardening parameters for 17–4PH stainless steel by artificial neural network and genetic algorithm, Mater. Sci. Eng., A 675 (2016) 147–152.
[40] S. Kotha, D. Ozturk, S. Ghosh, Parametrically homogenized constitutive models (PHCMs) from micromechanical crystal plasticity FE simulations, part I: Sensitivity analysis and parameter identification for Titanium alloys, Int. J. Plast. 120 (2019) 296–319.
[41] A. Rovinelli, M.D. Sangid, H. Proudhon, W. Ludwig, Using machine learning and a data-driven approach to identify the small fatigue crack driving force in polycrystalline materials, npj Comput. Mater. 4 (1) (2018).
[42] E. Ford, K. Maneparambil, S. Rajan, N. Neithalath, Machine learning-based accelerated property prediction of two-phase materials using microstructural descriptors and finite element analysis, Comput. Mater. Sci. 191 (2021) 110328.
[43] E. Westphal, H. Seitz, A machine learning method for defect detection and visualization in selective laser sintering based on convolutional neural networks, Addit. Manuf. 41 (2021) 101965.
[44] B. Zhang, S. Liu, Y.C. Shin, In-Process monitoring of porosity during laser additive manufacturing process, Addit. Manuf. 28 (2019) 497–505.
[45] A. Cecen, H. Dai, Y.C. Yabansu, S.R. Kalidindi, L. Song, Material structure-property linkages using three-dimensional convolutional neural networks, Acta Mater. 146 (2018) 76–84.
[46] J. Jung, J.I. Yoon, H.K. Park, J.Y. Kim, H.S. Kim, An efficient machine learning approach to establish structure-property linkages, Comput. Mater. Sci. 156 (2019) 17–25.
[47] A.L. Frankel, R.E. Jones, C. Alleman, J.A. Templeton, Predicting the mechanical response of oligocrystals with deep learning, Comput. Mater. Sci. 169 (2019) 109099.
[48] M. Yuan, S. Paradiso, B. Meredig, S.R. Niezgoda, Machine learning-based reduce order crystal plasticity modeling for ICME applications, Integr. Mater. Manuf. Innov. 7 (4) (2018) 214–230.
[49] A. Yamanaka, R. Kamijyo, K. Koenuma, I. Watanabe, T. Kuwabara, Deep neural network approach to estimate biaxial stress-strain curves of sheet metals, Mater. Des. 195 (2020) 108970.
[50] A. Mangal, E.A. Holm, Applied machine learning to predict stress hotspots II: Hexagonal close packed materials, Int. J. Plast. 114 (2019) 1–14.
[51] ASTM International. E606/E606M-21 Standard Test Method for Strain-Controlled Fatigue Testing. West Conshohocken, PA, 2021.
[52] M. Groeber, M. Jackson, Dream. 3D: A digital representation environment for the analysis of microstructure in 3D, Integr. Mater. Manuf. Innov. 3 (1) (2014) 1–17.
[53] ABAQUS, Dassault Systèmes Simulia Corp.
[54] N.M. Harrison, P.F. McDonnell, D.C. O'Mahoney, O.D. Kennedy, F.J. O'Brien, P.E. McHugh, Heterogeneous linear elastic trabecular bone modelling using micro-CT attenuation data and experimentally measured heterogeneous tissue properties, J. Biomech. 41 (11) (2008) 2589–2596.
[55] J.H. Friedman, The elements of statistical learning: Data mining, inference, and prediction, springer open2017.
[56] D. Systèmes, ABAQUS Documentation.
[57] W.G. Feather, H. Lim, M. Knezevic, A numerical study into element type and mesh resolution for crystal plasticity finite element modeling of explicit grain structures, Comput. Mech. 67 (1) (2021) 33–55.
[58] P.J. Ashton, A.M. Harte, S.B. Leen, Statistical grain size effects in fretting crack initiation, Tribol. Int. 108 (2017) 75–86.
[59] Y. Huang, A user-material subroutine incroporating single crystal plasticity in the ABAQUS finite element program, Harvard Univ, 1991.
[60] C.A. Sweeney, P.E. McHugh, J.P. McGarry, S.B. Leen, Micromechanical methodology for fatigue in cardiovascular stents, Int. J. Fatigue 44 (2012) 202–216.
[61] K. Shoemake, III.5. - Euler Angle Conversion, in: P.S. Heckbert (Ed.), Graphics Gems, Academic Press, 1994, pp. 222-229.
[62] K.M.K. Anthony Kelly, Appendix 5: Slip Systems in C.C.P. and B.C.C. Crystals, Crystallography and Crystal Defects, Wiley, 2012, pp. 481–486.
[63] A. Manonukul, F.P.E. Dunne, High– and low–cycle fatigue crack initiation using polycrystal plasticity, Proc. Roy. Soc. London. Series A: Math., Phys. Eng. Sci. 460(2047) (2004) 1881–1903.
[64] F.P.E. Dunne, Fatigue crack nucleation: Mechanistic modelling across the length scales, Curr. Opin. Solid State Mater. Sci. 18 (4) (2014) 170–179.
[65] D.L. McDowell, F.P.E. Dunne, Microstructure-sensitive computational modeling of fatigue crack formation, Int. J. Fatigue 32 (9) (2010) 1521–1542.
[66] A. Cruzado, S. Lucarini, J. Llorca, J. Segurado, Crystal plasticity simulation of the effect of grain size on the fatigue behavior of polycrystalline Inconel 718, Int. J. Fatigue 113 (2018) 236–245.
[67] A. Cruzado, S. Lucarini, J. Llorca, J. Segurado, Microstructure-based fatigue life model of metallic alloys with bilinear Coffin-Manson behavior, Int. J. Fatigue 107 (2018) 40–48.
[68] P.J. Ashton, Micromechanical modelling of size effects in crack initiation with application to fretting fatigue and cold dwell fatigue PhD Thesis, Mechanical Engineering, National University of Ireland, Galway, NUI Galway, 2018.
[69] C.A. Sweeney, B. O'Brien, P.E. McHugh, S.B. Leen, Experimental characterisation for micromechanical modelling of CoCr stent fatigue, Biomaterials 35 (1) (2014) 36–48.
[70] J.A. Grogan, S.B. Leen, P.E. McHugh, Influence of statistical size effects on the plastic deformation of coronary stents, J. Mech. Behav. Biomed. Mater. 20 (2013) 61–76.
[71] A. Zhang, Z.C. Lipton, M. Li, A.J. Smola, Dive into deep learning, arXiv preprint arXiv:2106.11342 (2021).
[72] Z. Zhang, Artificial Neural Network, in: Z. Zhang (Ed.), Multivariate Time Series Analysis in Climate and Environmental Research, Springer International Publishing, Cham, 2018, pp. 1–35.
[73] D. Chicco, Siamese Neural Networks: An Overview, in: H. Cartwright (Ed.), Artificial Neural Networks, Springer US, New York, NY, 2021, pp. 73–94.
[74] J. Wu, Introduction to convolutional neural networks, National Key Lab for Novel Software Technology. Nanjing University. China 5(23) (2017) 495.
[75] S. Albawi, T.A. Mohammed, S. Al-Zawi, Understanding of a convolutional neural network, 2017 International Conference on Engineering and Technology (ICET), 2017, pp. 1-6.
[76] M. Abadi, A. Agarwal, P. Barham, E. Brevdo, Z. Chen, C. Citro, G.S. Corrado, A. Davis, J. Dean, M. Devin, Tensorflow: Large-scale machine learning on heterogeneous distributed systems, arXiv preprint arXiv:1603.04467 (2016).
[77] J. Masci, M.M. Bronstein, A.M. Bronstein, J. Schmidhuber, Multimodal similarity-preserving hashing, IEEE Trans. Pattern Anal. Mach. Intell. 36 (4) (2014) 824–830.
[78] A. Gulli, A. Kapoor, S. Pal, Deep learning with TensorFlow 2 and Keras: regression, ConvNets, GANs, RNNs, NLP, and more with TensorFlow 2 and the Keras API, Packt Publishing Ltd, 2019.
[79] D.-F. Li, B.J. Golden, N.P. O'Dowd, Multiscale modelling of mechanical response in a martensitic steel: A micromechanical and length-scale-dependent framework for precipitate hardening, Acta Mater. 80 (2014) 445–456.
[80] V. Herrera-Solaz, L. Patriarca, S. Foletti, J. Segurado, M. Niffenegger, Microstructure-based modelling and Digital Image Correlation measurement of strain fields in austenitic stainless steel 316L during tension loading, Mater. Sci. Eng., A (2019).
[81] K. Kapoor, Y.S.J. Yoo, T.A. Book, J.P. Kacher, M.D. Sangid, Incorporating grain-level residual stresses and validating a crystal plasticity model of a two-phase Ti-6Al-4 V alloy produced via additive manufacturing, J. Mech. Phys. Solids 121 (2018) 447–462.
[82] J. Suryawanshi, K.G. Prashanth, U. Ramamurty, Mechanical behavior of selective laser melted 316L stainless steel, Mater. Sci. Eng., A 696 (2017) 113–121.
[83] Y.J. Yin, J.Q. Sun, J. Guo, X.F. Kan, D.C. Yang, Mechanism of high yield strength and yield ratio of 316 L stainless steel by additive manufacturing, Mater. Sci. Eng., A 744 (2019) 773–777.
[84] M.S. Pham, B. Dovgyy, P.A. Hooper, Twinning induced plasticity in austenitic stainless steel 316L made by additive manufacturing, Mater. Sci. Eng., A 704 (2017) 102–111.
[85] K. Guan, Z. Wang, M. Gao, X. Li, X. Zeng, Effects of processing parameters on tensile properties of selective laser melted 304 stainless steel, Mater. Des. 50 (2013) 581–586.
[86] X.H. Hu, X. Sun, L.G. Hector, Y. Ren, Individual phase constitutive properties of a TRIP-assisted QP980 steel from a combined synchrotron X-ray diffraction and crystal plasticity approach, Acta Mater. 132 (2017) 230–244.
[87] M. Yaghoobi, K.S. Stopka, A. Lakshmanan, V. Sundararaghavan, J.E. Allison, D.L. McDowell, PRISMS-Fatigue computational framework for fatigue analysis in polycrystalline metals and alloys, npj Comput. Mater. 7 (1) (2021) 38.
[88] P.G.E. Jerrard, L. Hao, K.E. Evans, Experimental investigation into selective laser melting of austenitic and martensitic stainless steel powder mixtures, Proc. Instit. Mech. Eng., Part B: J. Eng. Manuf. 223 (11) (2009) 1409–1416.

[89] X. Yang, R.A. Barrett, M. Tong, N.M. Harrison, S.B. Leen, Prediction of microstructure evolution for additive manufacturing of Ti-6Al-4V, Procedia Manuf. 47 (2020) 1178–1183.

[90] X. Yang, R.A. Barrett, M. Tong, N.M. Harrison, S.B. Leen, Towards a process-structure model for Ti-6Al-4V during additive manufacturing, J. Manuf. Processes 61 (2021) 428–439.